Supporting information for

Simultaneous band gap narrowing and carrier lifetime prolongation of organic-inorganic trihalide perovskites

Lingping Kong[a,b], Gang Liu[a,b,1], Jue Gong[c], Qingyang Hu[a,b], Richard D. Schaller[d], Przemyslaw Dera[e], Dongzhou Zhang[e], Zhenxian Liu[b], Wenge Yang[a,b], Kai Zhu[f], Yuzhao Tang[g], Chuanyi Wang[h], Su-Huai Wei[i], Tao Xu[c,1] and Ho-kwang Mao[a,b,1]

[a]Center for High Pressure Science and Technology Advanced Research, Shanghai 201203, China

[b]Geophysical Laboratory, Carnegie Institution of Washington, Washington, DC 20015, USA.

[c]Department of Chemistry and Biochemistry, Northern Illinois University, DeKalb, IL 60115, USA.

[d]Center for Nanoscale Materials, Argonne National Laboratory, Argonne, IL 60439, USA.

[e]Hawai'i Institute of Geophysics and Planetology, School of Ocean and Earth Science and Technology, University of Hawai'i at Manoa, Honolulu, HI 96822, USA.

[f]Chemistry and Nanoscience Center, National Renewable Energy Laboratory, Golden, CO 80401, USA.

[g]National Center for Protein Science Shanghai, Institute of Biochemistry and Cell Biology, Shanghai Institutes for Biological Sciences, Chinese Academy of Sciences, Shanghai 201210, China

[h]Xinjiang Technical Institute of Physics and Chemistry, Chinese Academy of Sciences, Urumqi 830011, China

[i]Beijing Computational Science Research Center, Beijing 100193, China

[1]To whom correspondence should be addresseds. E-mail: liugang@hpstar.ac.cn (G.L); txu@niu.edu (T.X); hmao@carnegiescience.edu (H-k.M).

Contents

SI Section 1. Crystal structure characterization at ambient condition.

1.1 Synchrotron high resolution powder X-ray diffraction.

Structure solution and refinement in the space group *I4/mcm* were performed for $MAPbI_3$, without difficulties, while the XRD pattern of $MAPbBr_3$ can be well satisfied by the single phase model of $Pm\bar{3}m$. Our results are well consistent with previous structural investigations (1, 2). Figs. S1-S2 shows the high resolution synchrotron XRD profiles and GSAS refinement results for $MAPbI_3$ and $MAPbBr_3$, respectively, and structural parameters are listed in Tables S1-S2.

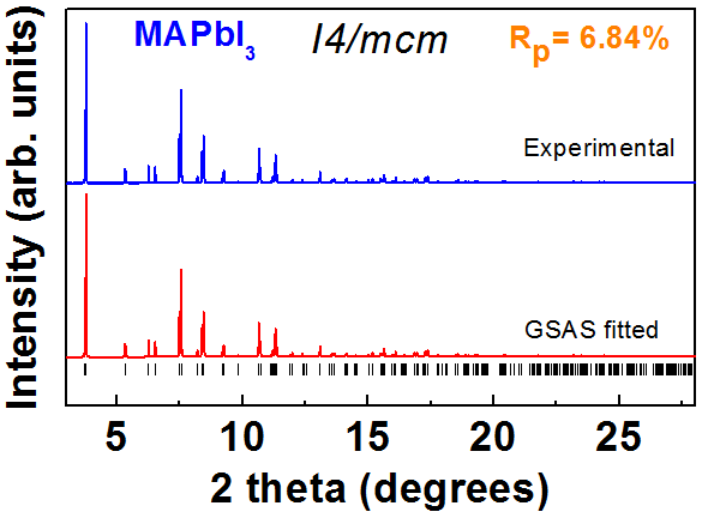

Figure S1. Synchrotron high resolution angle dispersive X-ray powder diffraction pattern of $MAPbI_3$ and GSAS fitted results. Bragg reflections of *I4/mcm* space group are indicated by black vertical bars "|".

Table S1. Refined lattice parameters for $MAPbI_3$ derived from synchrotron high resolution powder X-ray diffraction at room temperature.

Materials	Crystal system	Space group	Lattice parameters (Å)	Ref.
$MAPbI_3$	Tetragonal	*I4/mcm* (no. 140)	$a = b = 8.8706$ (2); $c = 12.6707$ (4)	This work
$MAPbI_3$	Tetragonal	*I4/mcm* (no. 140)	$a = b = 8.8743$ (4); $c = 12.6708$ (5)	1

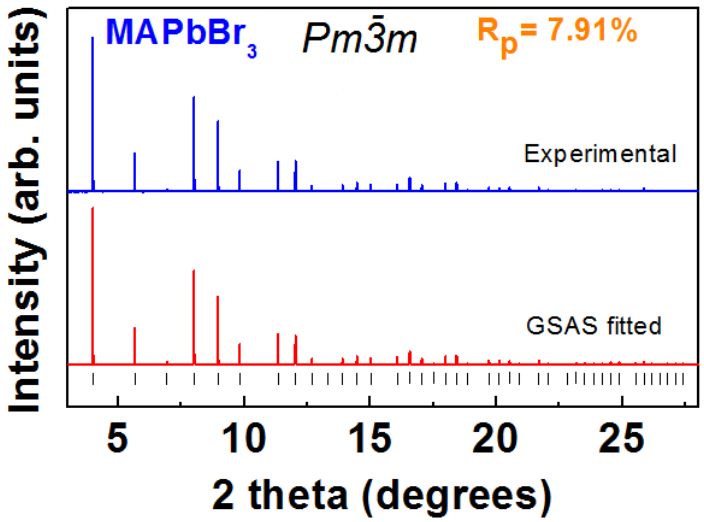

Figure S2. Synchrotron high resolution angle dispersive X-ray powder diffraction pattern of $MAPbBr_3$ and GSAS fitted results. Bragg reflections of the space group $Pm\bar{3}m$ are indicated by black vertical bars "|".

Table S2. Refined lattice parameters for $MAPbBr_3$ derived from synchrotron high resolution powder X-ray diffraction at room temperature.

Materials	Crystal system	Space group	Lattice parameters (Å)	Ref.
$MAPbBr_3$	Cubic	$Pm\bar{3}m$ (no. 221)	$a = b$ = c= 5.9291 (1)	This work
$MAPbBr_3$	Cubic	$Pm\bar{3}m$ (no. 221)	$a = b$ = c= 5.9313 (4)	2

1.2 Synchrotron single crystal X-ray diffraction.

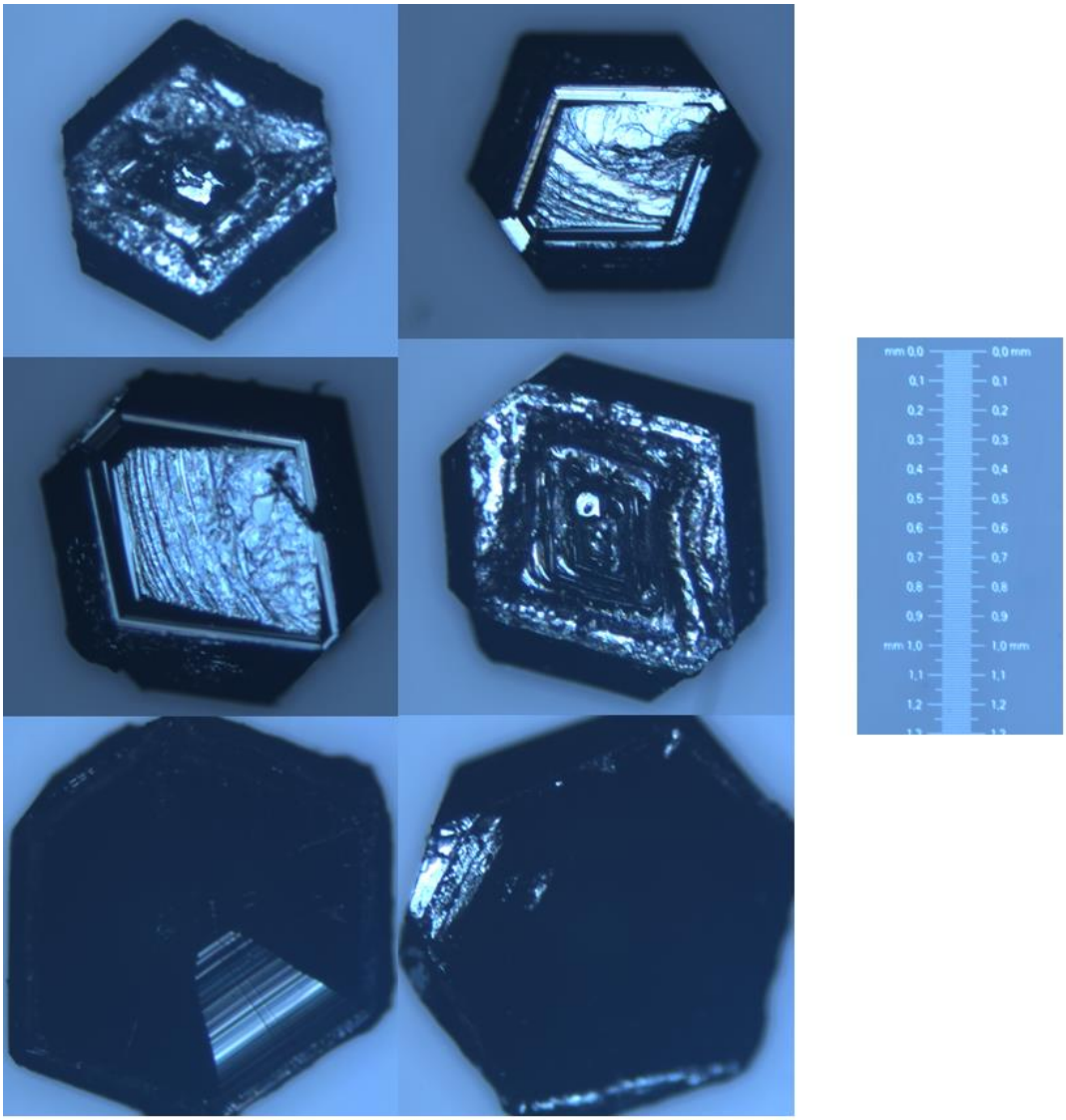

Figure S3. Photographs of as-grown $MAPbI_3$ single crystals.

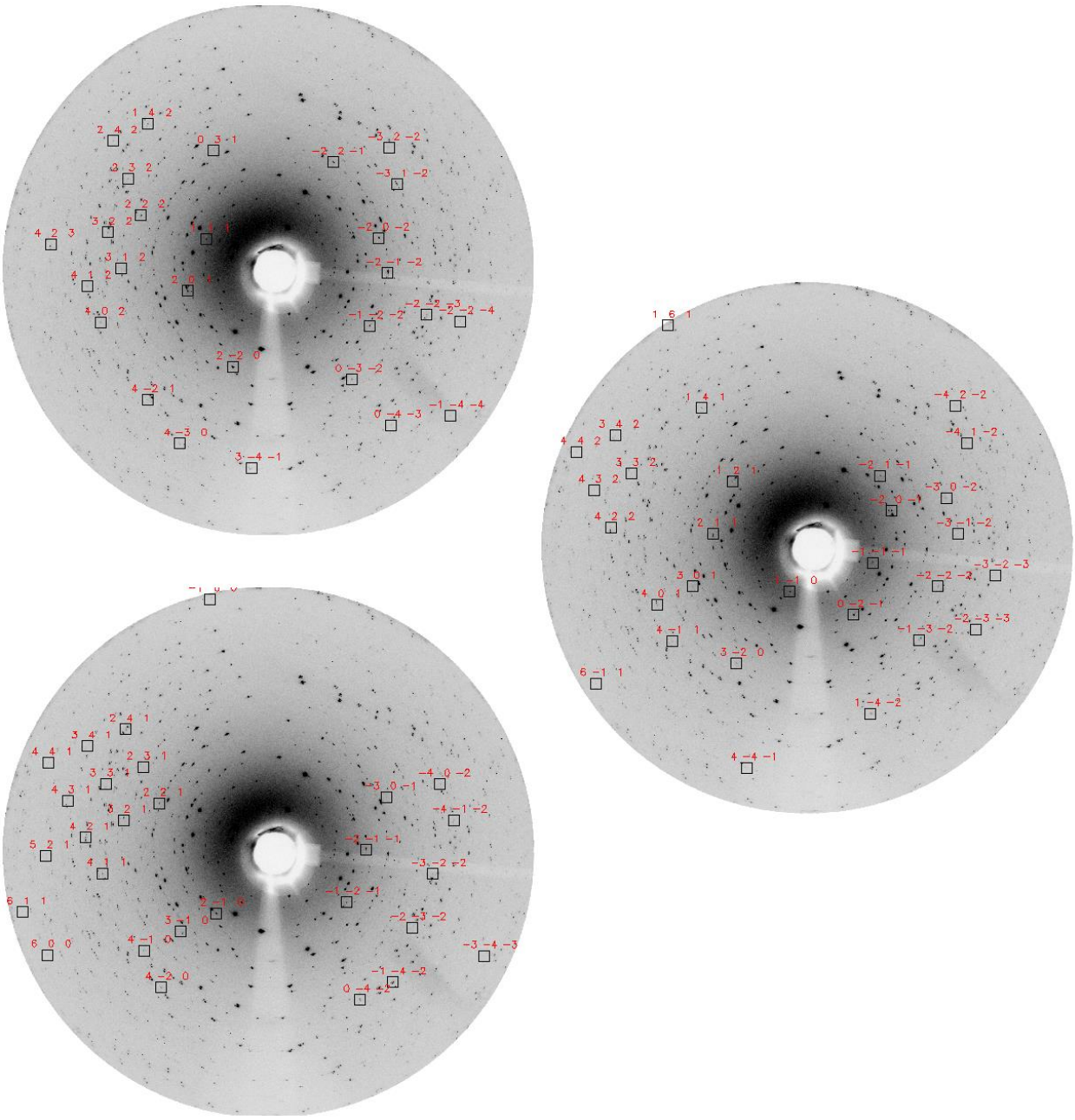

Figure S4. Diffraction pattern for $MAPbI_3$ single crystal collected at an ambient condition (1 atm, room temperature) at the center detector position. Diffraction reflections are indexed using the *I4/mcm* space group model.

Table S3. $MAPbI_3$ crystal data and structure refinement for the ambient pressure phase.

Identification code	Shelxl
Temperature	293(2) K
Wavelength	0.43400 Å
Crystal system, space group	Tetragonal, *I4/mcm*
Unit cell dimensions	a = 8.8670(8) Å b = 8.8670(8) Å c = 12.676(2) Å
Volume	996.63(4) $Å^3$
Theta range for data collection	-90 to 90 degree
Limiting indices	-12<=h<=13, -12<=k<=18, -5<=l<=0
Refinement method	Full-matrix least-squares on F^2
Goodness-of-fit on F^2	1.233
Final R indices [I>2sigma(I)]	R_1 = 0.0453, wR_2= 0.0941
R indices (all data)	R_1 = 0.0491, wR_2 = 0.0944

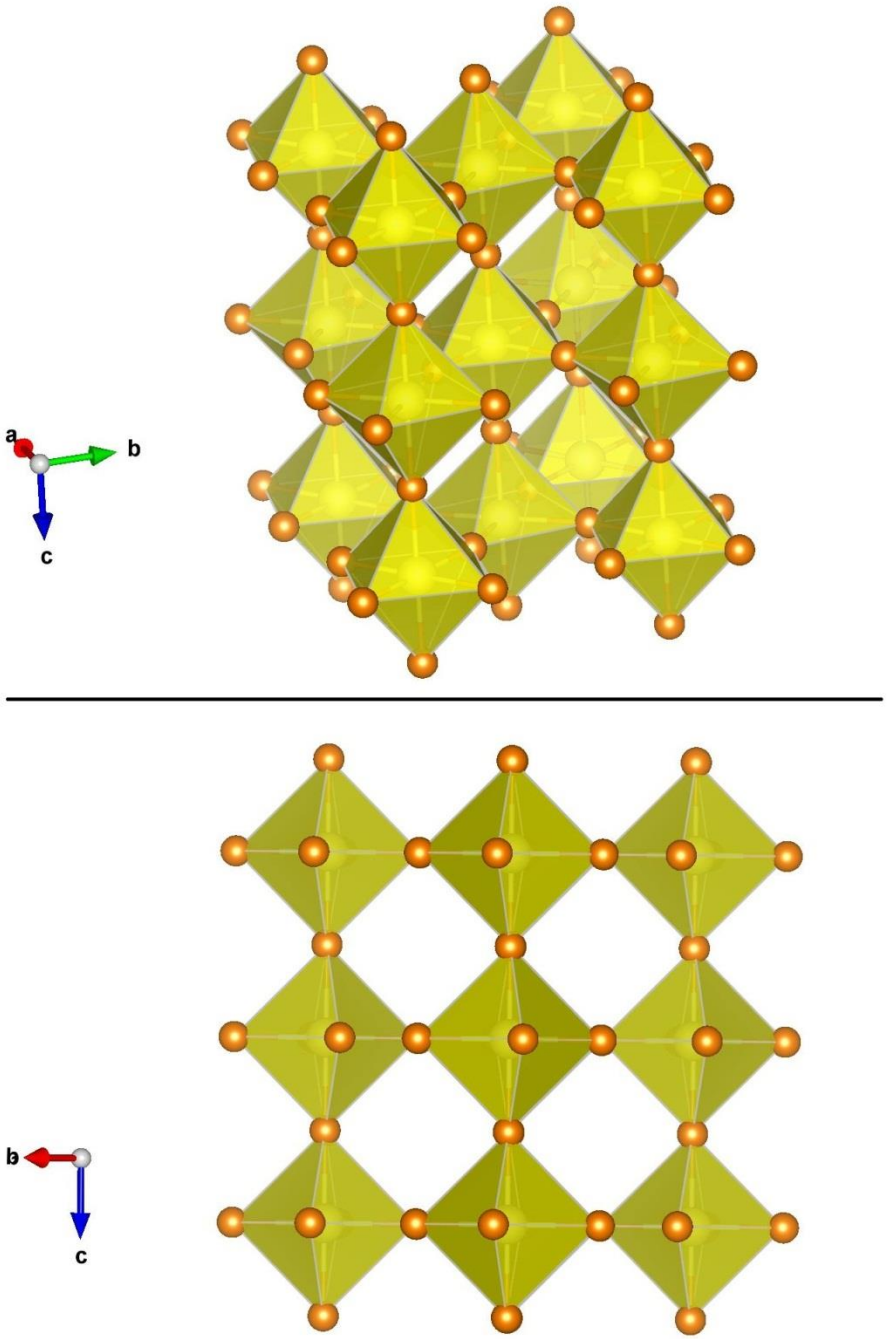

Figure S5. Schematic crystal structure of $MAPbI_3$ at an ambient condition. Orange spherical balls stand for I and Pb-I octahedral are highlighted with dark yellow.

SI Section 2. High pressure crystal structure characterization.

2.1 *In-situ* synchrotron powder X-ray diffraction under various pressures.

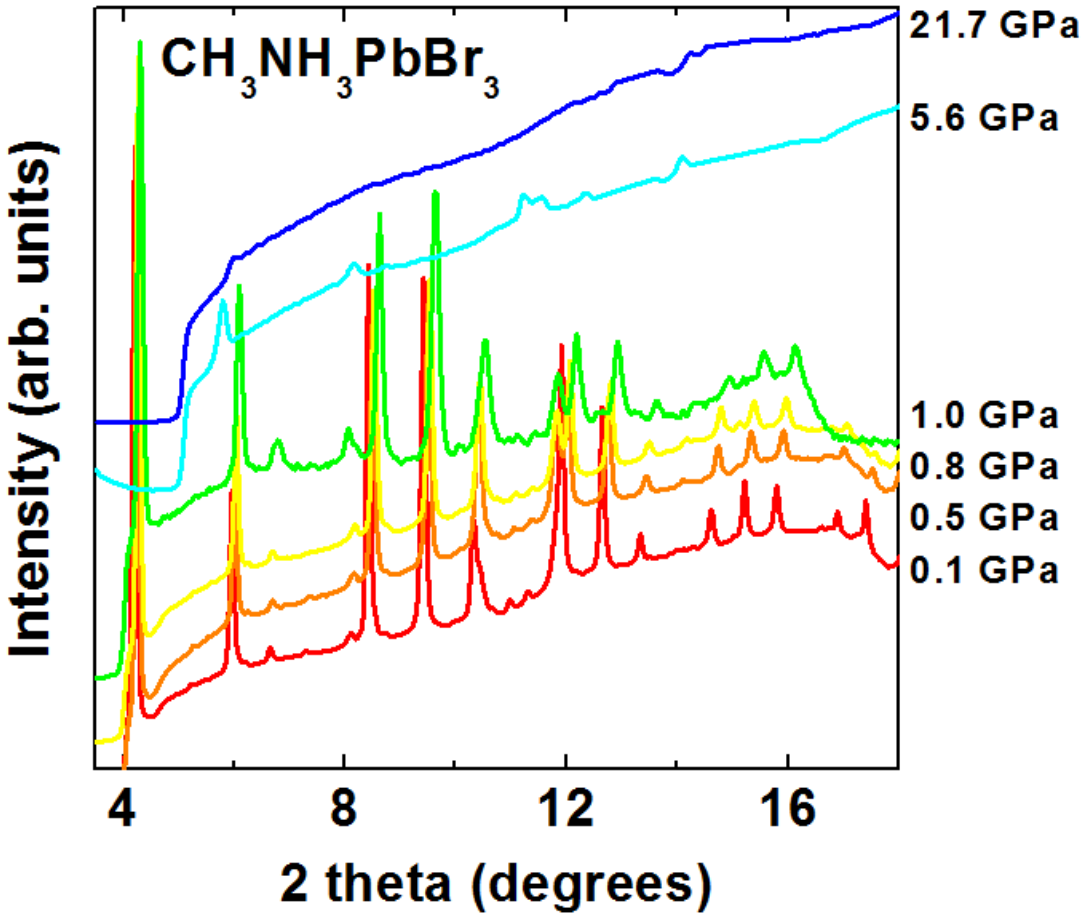

Figure S6. *In-situ* high pressure XRD characterization of $MAPbBr_3$: pressure dependent angle dispersive X-ray diffraction patterns in compression up to 21.7 GPa. As the pressure increases, the $Pm\bar{3}m \rightarrow Im\bar{3}$ phase transition occurs. Note that both the ambient structure ($Pm\bar{3}m$) and high pressure phase $Im\bar{3}$ belong to cubic symmetry. Based on the GSAS refinement results shown in Figs. S7-S10, this structural evolution exhibits a dynamic characteristic, which can be demonstrated by the co-existence of the $Pm\bar{3}m$ and $Im\bar{3}$ phases at 0.5 GPa. In addition, pressure induced amorphization was observed at 5.6 GPa from the broad XRD profile.

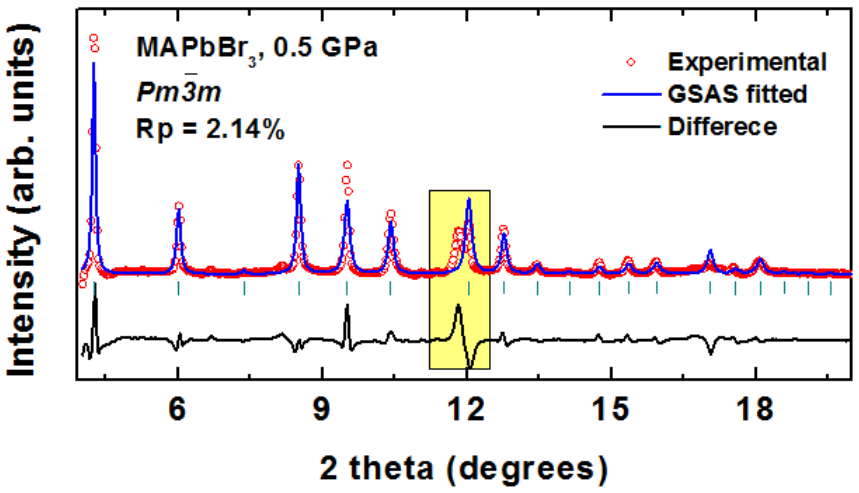

Figure S7. GSAS refinement of the XRD pattern of $MAPbBr_3$ measured at 0.5 GPa using $Pm\bar{3}m$ model, in which the section highlighted in yellow indicates that the XRD pattern cannot be satisfied by such a single phase**.** Bragg reflections of the space group $Pm\bar{3}m$ are indicated by dark green bars "|".

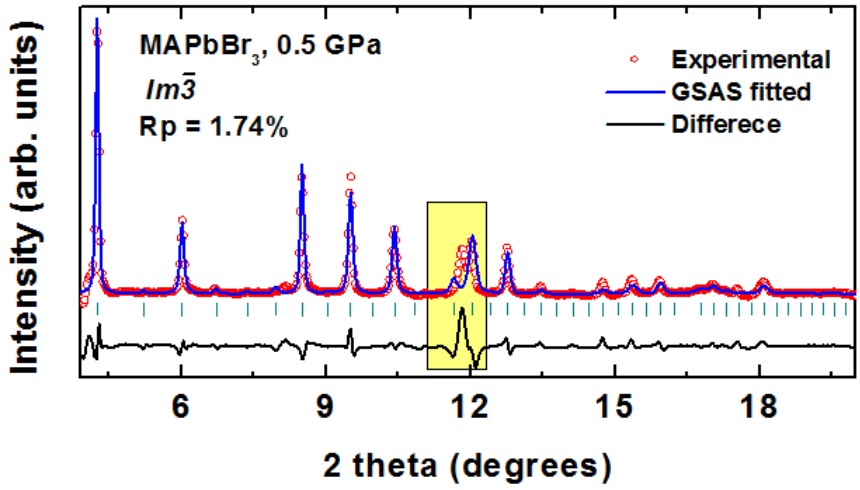

Figure S8. GSAS refinement of the XRD pattern of $MAPbBr_3$ measured at 0.5 GPa using $Im\bar{3}$ model, in which the section highlighted in yellow indicates that the XRD pattern cannot be satisfied by such a single phase**.** Bragg reflections of the space group $Im\bar{3}$ are indicated by dark green bars "|".

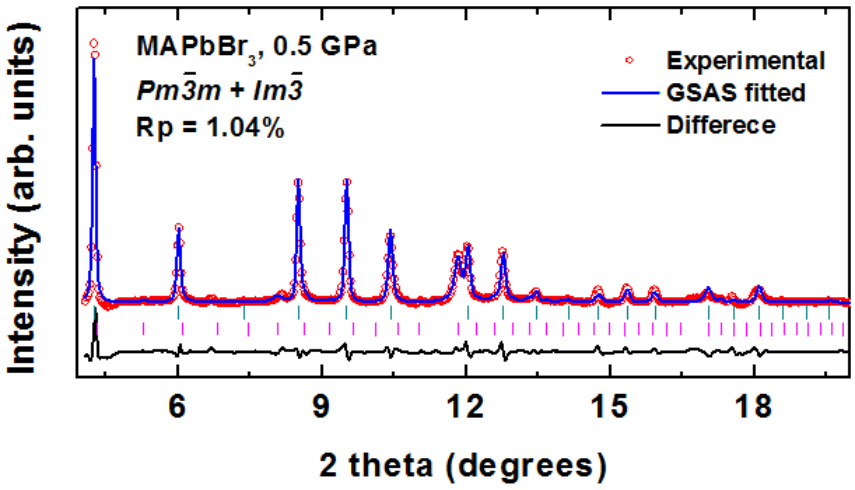

Figure S9. GSAS refinement of the XRD pattern of $MAPbBr_3$ measured at 0.5 GPa using the $Pm\bar{3}m$ +$Im\bar{3}$ mix-phase model, reveals the real structure. Bragg reflections of the space group $Pm\bar{3}m$ and $Im\bar{3}$ are indicated by dark green and pink bars, respectively.

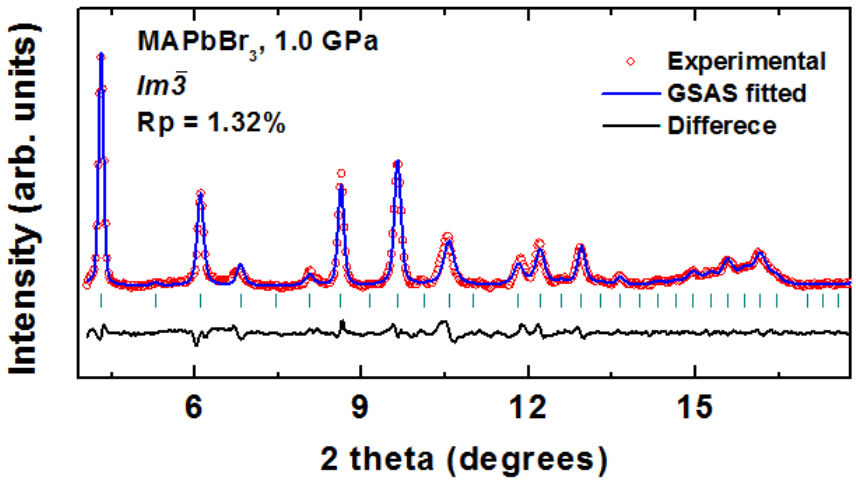

Figure S10. GSAS refinement of the XRD pattern of $MAPbBr_3$ measured at 1.0 GPa using $Im\bar{3}$ model. Bragg reflections of the space group $Im\bar{3}$ are indicated by dark green bars. Considering the results shown in Figs. S3, S9, and S10, the phase transition sequence of $Pm\bar{3}m \rightarrow Pm\bar{3}m$+$Im\bar{3} \rightarrow Im\bar{3}$ can be concluded and the high pressure $Im\bar{3}$ phase clearly occurs at 0.5 GPa.

2.2 *In-situ* synchrotron single crystal X-ray diffraction at pressures.

Indexing of data of $MAPbI_3$ at 0.4 GPa revealed a single lattice with a=12.408(3) Å, b=12.419(3) Å, c=12.25(4) Å unit cell (2×2×2 supercell of the primitive-cubic perovskite cell). Metrically, this unit cell is approximately tetragonal and our analysis of systematic absences showed no indication of the presence of glide planes or screw axes. However, based on our merging statistics analysis conducted with the XPREP program (3), the crystal system cannot be clearly resolved using any space group belonging to the tetragonal symmetry as an initial mode. Therefore, we sought to identify the structure model in an orthorhombic system instead. We further examined space groups *Pmmm*, *P222* and *Imm2* and investigated their simulated annealing structures. However, only calculations in the *Imm2* space group gave a promising initial model, which was eventually refined with ShelXL program (3) against the single crystal data and yielded a satisfactory 6.5% refinement reliability factor R_1 with the 348 observed peak intensities used. Similar to the *I4/mcm* phase at pressure < 0.4 GPa, this *Imm2* structure obtained at pressures >0.4 GPa exhibited only one symmetrically independent Pb site, whereas the original two iodine sites split into five sites (one 8e, two 4d and 4c in Wyckoff classification).

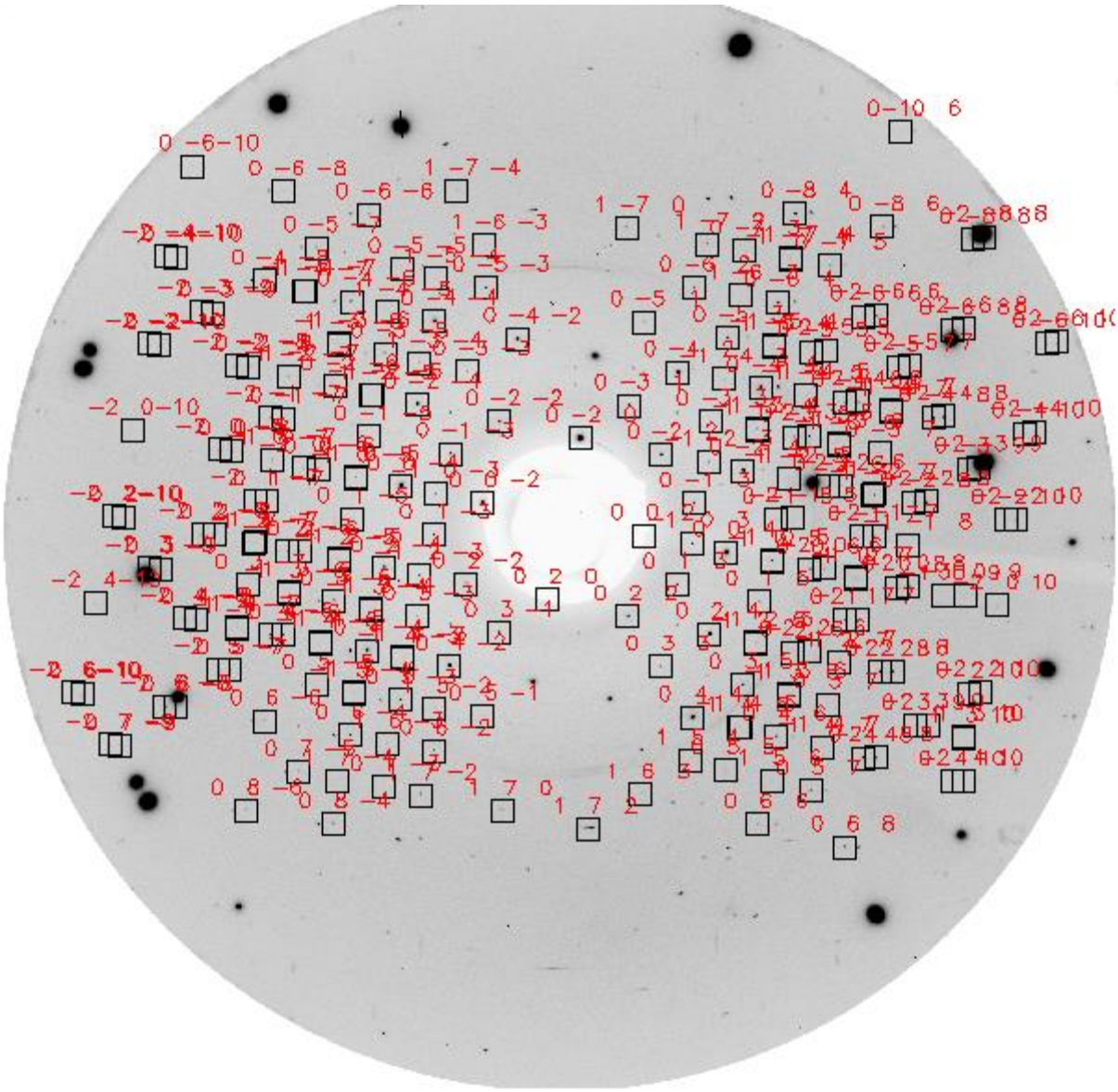

Figure S11. Diffraction pattern for $MAPbI_3$ single crystal collected at 0.4 GPa at the center detector position. Diffraction reflections are indexed using the *Imm2* space group model.

Table S4. $MAPbI_3$ crystal data and structure refinement for high pressure phase at 0.4 GPa.

Identification code	Shelxl
Temperature	293(2) K
Wavelength	0.43400 Å
Crystal system, space group	Orthorhombic, *Imm2*
Unit cell dimensions	a = 12.408(3) Å b = 12.419(3) Å c = 12.25(5) Å
Volume	1888(8) $Å^3$
Theta range for data collection	3.07 to 15.65 degree
Limiting indices	-12<=h<=13, -12<=k<=18, -5<=l<=0
Reflections collected / unique	348 / 348 [R(int) = 0.0000]
Completeness to theta = 15.65	7.3 %
Refinement method	Full-matrix least-squares on F^2
Data / restraints / parameters	348 / 1 / 21
Goodness-of-fit on F^2	1.189
Final R indices [I>2sigma(I)]	R_1 = 0.0647, wR_2 = 0.1745
R indices (all data)	R_1 = 0.0869, wR_2 = 0.1746
Largest diff. peak and hole	1.527 and -1.046 $e.A^{-3}$

Table S5. Atomic coordinates ($\times 10^4$) and equivalent isotropic displacement parameters ($A^2 \times 10^3$) for *Imm2*. U(eq) is defined as one third of the trace of the orthogonalized, Uij tensor.

	x	y	z	U(eq)
Pb(1)	2482(5)	2585(7)	2969(4)	27(2)
I(1)	2750(20)	2340(20)	4850(120)	207(12)
I(2)	0	1983(7)	7270(60	17(4)
I(3)	0	2388(10)	3390(50)	24(4)
I(4)	2415(10)	5000	3360(70)	35(4)
I(5)	2996(9)	0	2630(80)	28(3)

Table S6. Bond lengths [Å] and angles [deg] for *Imm2*.

Bond lengths [Å]	
Pb(1)-I(1)	2.340(15)
Pb(1)-I(4)	3.039(17)
Pb(1)-I(3)	3.132(11)
Pb(1)-I(2)#1	3.285(19)
Pb(1)-I(5)	3.298(11)
I(2)-Pb(1)#2	3.285(19)
I(2)-Pb(1)#3	3.285(19)
I(3)-Pb(1)#4	3.132(11)
I(4)-Pb(1)#5	3.039(17)
I(5)-Pb(1)#6	3.298(11)
Angles [deg]	
I(1)-Pb(1)-I(4)	88.8(16)
I(1)-Pb(1)-I(3)	88.2(15)
I(4)-Pb(1)-I(3)	91.4(4)
I(1)-Pb(1)-I(2)#1	98.2(15)
I(4)-Pb(1)-I(2)#1	84.6(6)
I(3)-Pb(1)-I(2)#1	172.3(13)
I(1)-Pb(1)-I(5)	88.1(17)
I(4)-Pb(1)-I(5)	170.3(5)
I(3)-Pb(1)-I(5)	97.7(4)
I(2)#1-Pb(1)-I(5)	86.7(4)
Pb(1)#2-I(2)-Pb(1)#3	144.0(20)
Pb(1)#4-I(3)-Pb(1)	159.0(21)
Pb(1)-I(4)-Pb(1)#5	162.0(32)
Pb(1)#6-I(5)-Pb(1)	153.4(17)

Symmetry transformations used to generate equivalent atoms:

#1 -x+1/2, -y+1/2, z-1/2 #2 -x+1/2, -y+1/2, z+1/2

#3 x-1/2, -y+1/2, z+1/2 #4 -x, y, z #5 x, -y+1, z

#6 x, -y, z

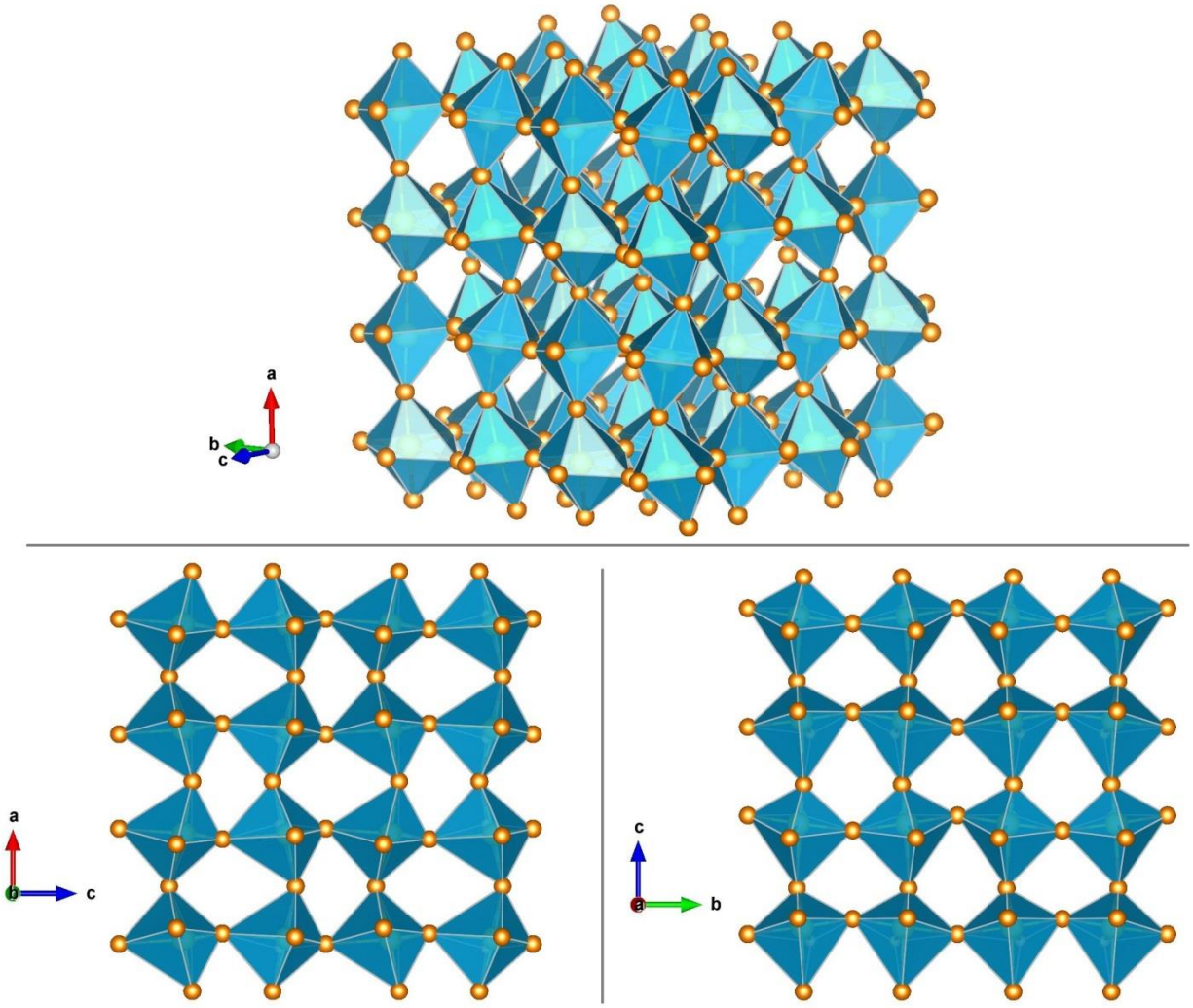

Figure S12. Schematic crystal structure of $MAPbI_3$ at 0.4 GPa. Orange spherical balls stand for I atoms and Pb-I octahedral are highlighted in blue.

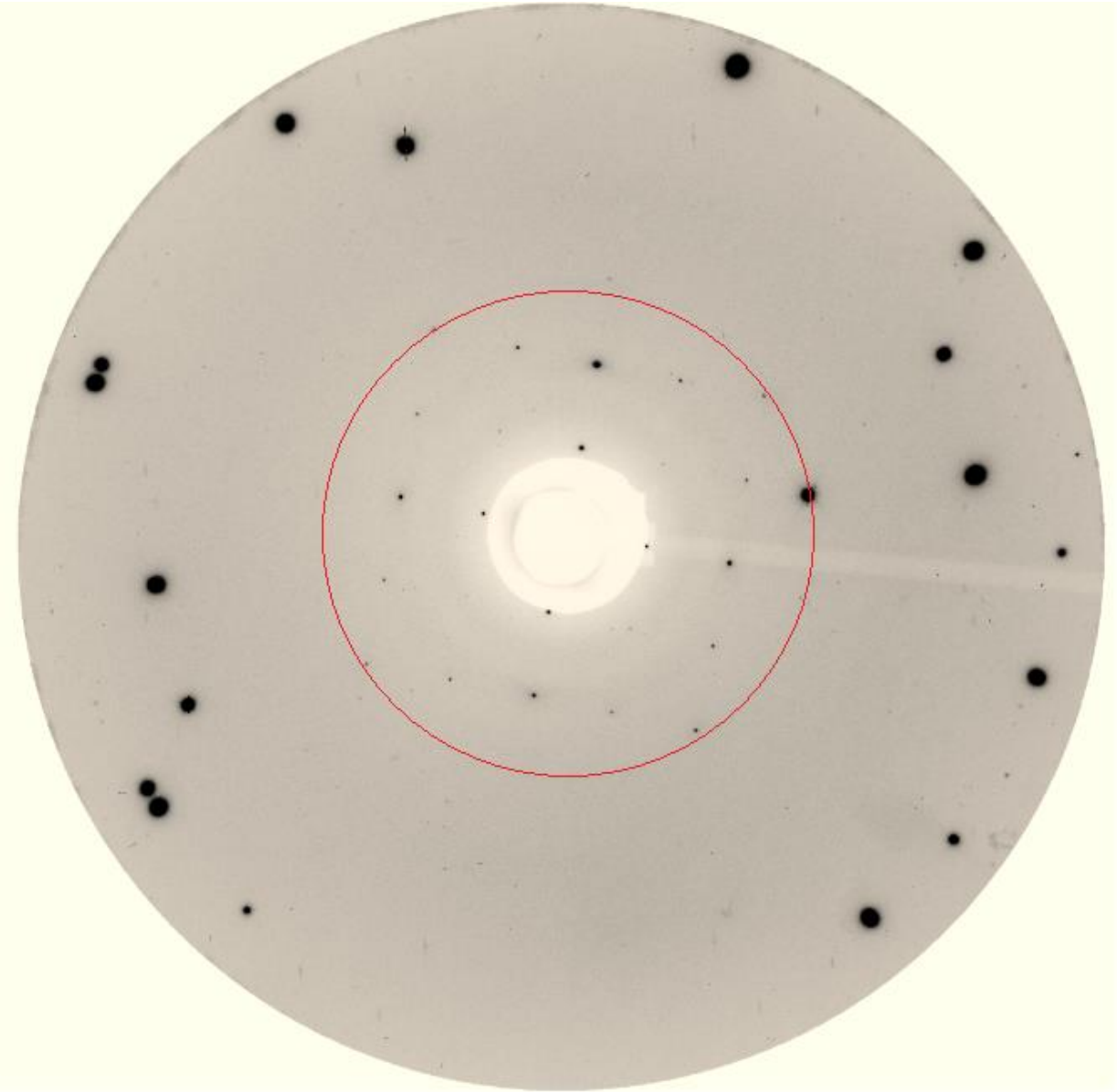

Figure S13. Diffraction pattern for $MAPbI_3$ single crystal collected at 4.6 GPa at the center detector position. Single crystal spots disappear and pressure induced amorphization can be concluded. Note that the big single crystal spots outside the red circle are from diamond.

SI Section 3. High pressure Raman spectra characterization.

Figs. S14-S15 show the high pressure Raman spectrum characterization for $MAPbBr_3$, and $MAPbI_3$ samples, respectively. For $MAPbBr_3$, both the ambient phase ($Pm\bar{3}m$) and high pressure phase ($Im\bar{3}$) are center inversion symmetry structures, thus first-order Raman scattering are forbidden (4). Therefore, Raman modes are inactive and cannot be observed as convinced in (Fig. S14). For $MAPbI_3$, the observed Raman mode is around 200~220 cm^{-1}, which can be assigned as the torsional mode of the methylammonium cations (MA^+) based on DFT simulations (5). As pressure increased from 1 atm to 0.1 GPa, a red shift of the torsional mode of the MA^+ from 218 cm^{-1} down to 202 cm^{-1} was observed for $MAPbI_3$, followed by a blue jump to 217 cm^{-1} at 0.4 GPa (see Fig. S15(B)). The difference in change of vibrational frequencies between low pressure (< 0.4 GPa) and the high pressure range demonstrates the existence of a distinct local structure of organic groups, which is further supported by our XRD experiments.

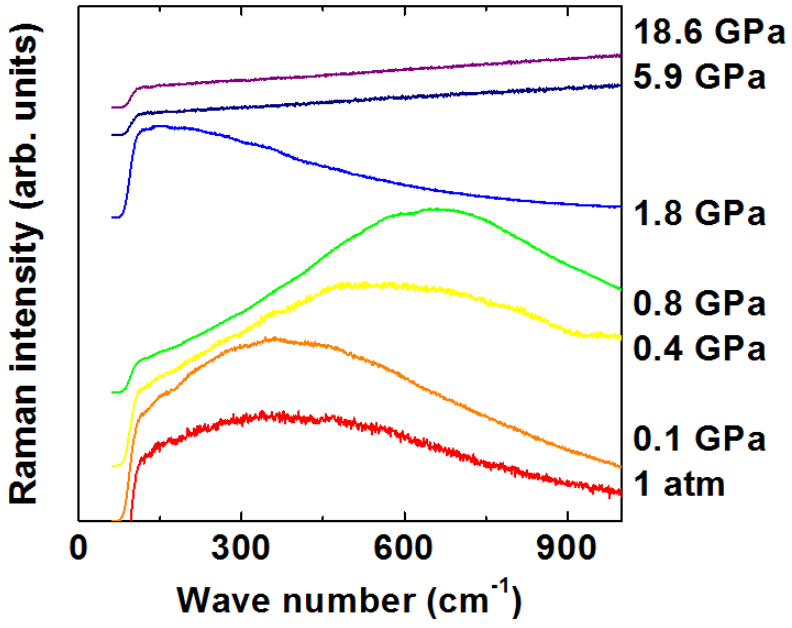

Figure S14. Pressure-dependent Raman spectra of $MAPbBr_3$ at selected pressures.

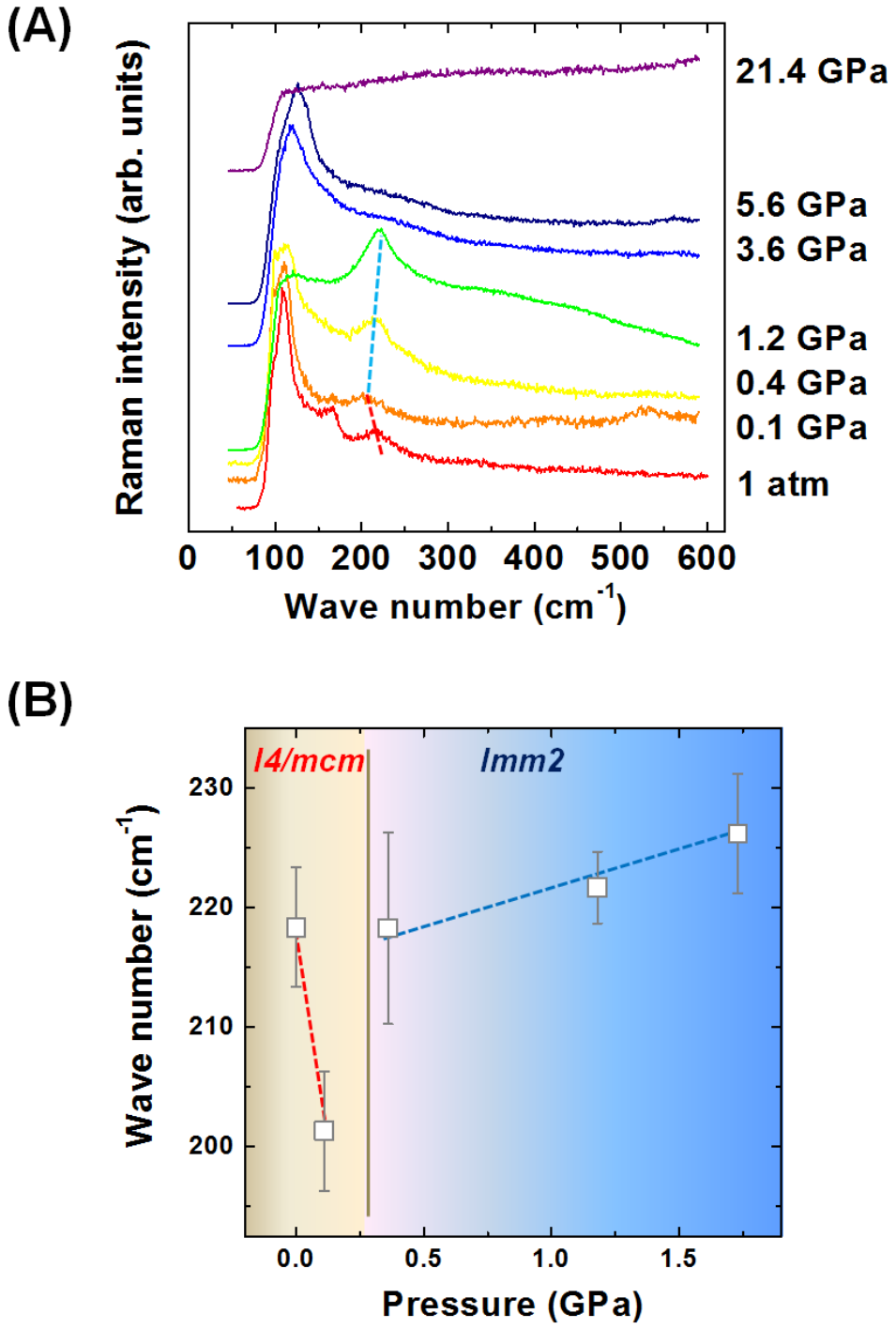

Figure S15. (A) Pressure-dependent Raman spectra of $MAPbI_3$ at selected pressures; (B) The pressure dependence of the MA^+ torsional Raman band. The regions of the low pressure phase *I4/mcm* and high pressure phase *Imm2* are highlighted with different color backgrounds.

SI Section 4. High pressure IR spectra characterization.

Pressure-driven structural evolution of $MAPbI_3$ can be further supported by *in-situ* high pressure mid-infrared (IR) measurements (Fig. S16). As pressure rises, vibrational peaks due to the organic moiety shift and broaden. This effect can be exactly elucidated by the intensified interatomic force, and the decrease in both the structural long-range order and crystallinity (6). Both blue-shifts and red-shifts are observed in characteristic modes (Figs. S17-S20). Explicitly, for the $-CH_3$ stretching mode (Fig. S17), no significant changes in frequency were observed in the low pressure phase (between 1 atm and 0.4 GPa) that exhibited the same space group *I4/mcm* as the ambient phase. However, a notable blue-shift was observed as pressure exceeded 0.4 GPa, from which the crystal phase transition started to occur. In these high pressure phases (*Imm2*), the volume of the lattice underwent considerable shrinkage, leading to strenuous repulsion between the inorganic PbI_3^- framework and the electron waves on the H atoms in the methyl group. Hence, the frequency of C-H stretching increased. The same rationale can also be applied to illustrate the blue-shift of the C-N stretch above 0.4 GPa (Fig. S18). In contrast, however, both the N-H stretching (Fig. S19) and bending (Fig. S20) modes in the NH_3^+ experienced red-shift as pressure increased. This opposite trend for N-H modes with respect to the C-H and C-N modes can be attributed to the cationic charge on $CH_3NH_3^+$, which is well-known to be localized to the three hydrogen atoms connecting to the nitrogen. Therefore, the pressure-induced lattice shrinkage further enhanced the electrostatic attraction between the cationic charge on the nearly naked protons in NH_3^+ and their neighboring anionic charge on the PbI_3^- framework. Conclusively, it is this attraction force that slows down the modes in NH_3^+. From the *in-situ* high pressure IR spectra of $MAPbBr_3$ (Fig. S21), we also observed both the pressure-driven blue-shift and red-shift in C-N stretch and NH3+ bending, respectively (Fig. S22).

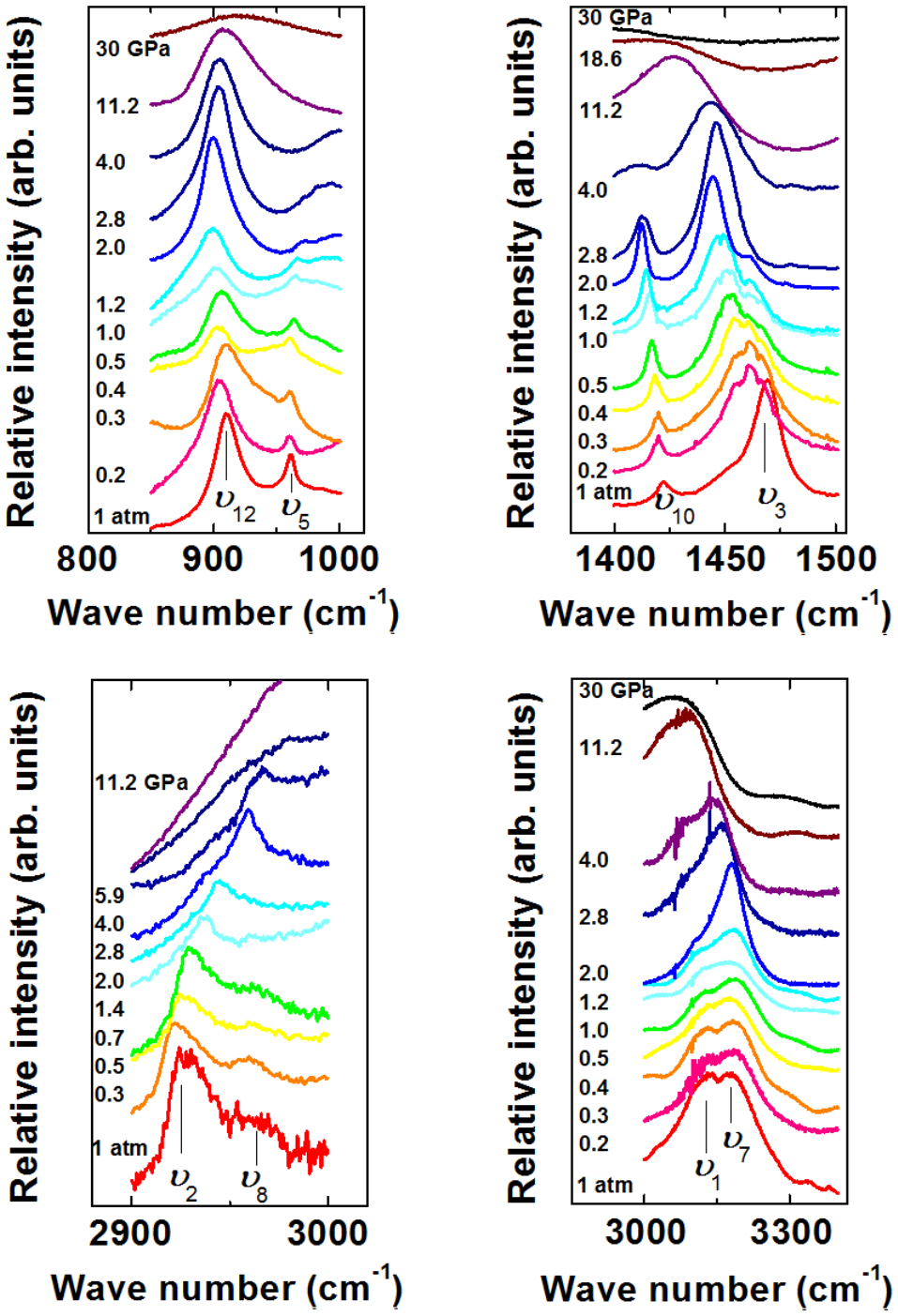

Figure S16. Pressure dependent mid-infrared spectra of $CH_3NH_3PbI_3$ single crystal up to 30 GPa. Under ambient pressure, C-N stretch (ν_5) has a frequency at around 962 cm^{-1}, asymmetric CH_3 bending (ν_{10}) at around 1422 cm^{-1}, symmetric CH_3 stretching (ν_2) at around 2925 cm^{-1},

symmetric NH_3^+ bending (v_3) at about 1470 cm^{-1}, asymmetric NH_3^+ stretching (v_7) at about 3180 cm^{-1}, CH_3-NH_3^+ rock (v_{12}) at around 911 cm^{-1}, asymmetric CH_3 stretching (v_8) at around 2962 cm^{-1}, and symmetric NH_3^+ stretching (v_1) at around 3129 cm^{-1}. These assignments agree well with the reported values (7-10). Numbering v_x of the peaks corresponds to the one given in ref. 7.

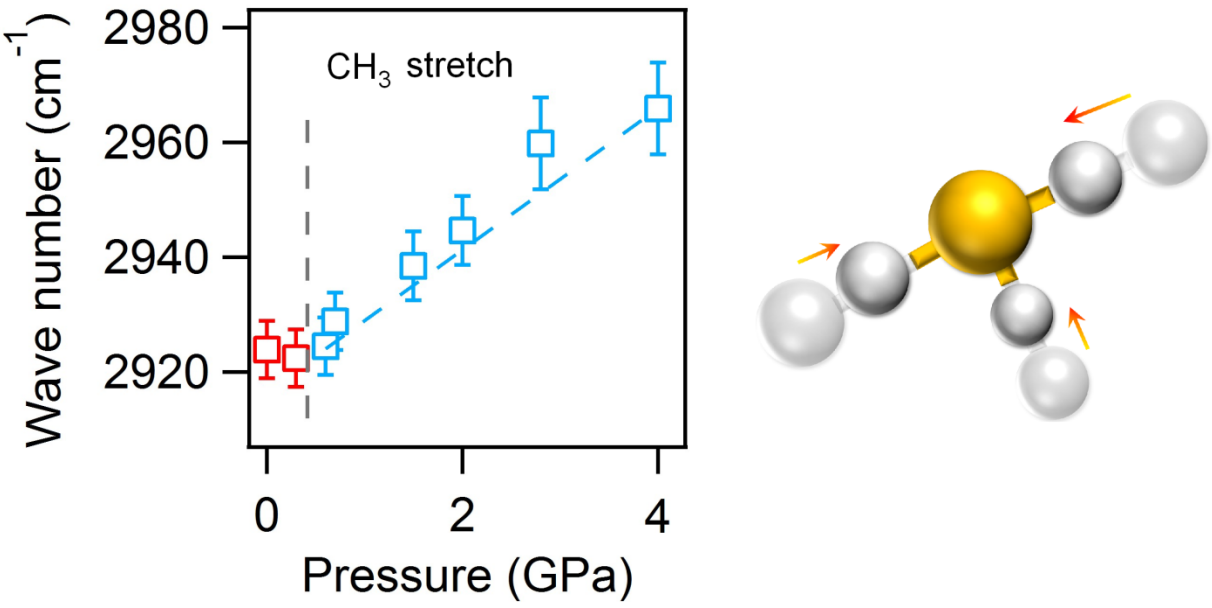

Figure S17. Pressure dependence of mid-IR CH_3 stretch mode. Pressure-driven IR peak shifts are distinct between low pressure and high pressure phase ranges. Red and blue open squares represent the peak positions of the IR modes measured in a low pressure range corresponding to the *I4/mcm* phase and in a high pressure range corresponding to the *Imm2* phase, respectively. Grey dash lines indicate the approximate phase boundaries. Blue dash line is the guide to the eyes for blue-shift in the IR mode. Errors are derived from the function fitting of IR absorption peaks.

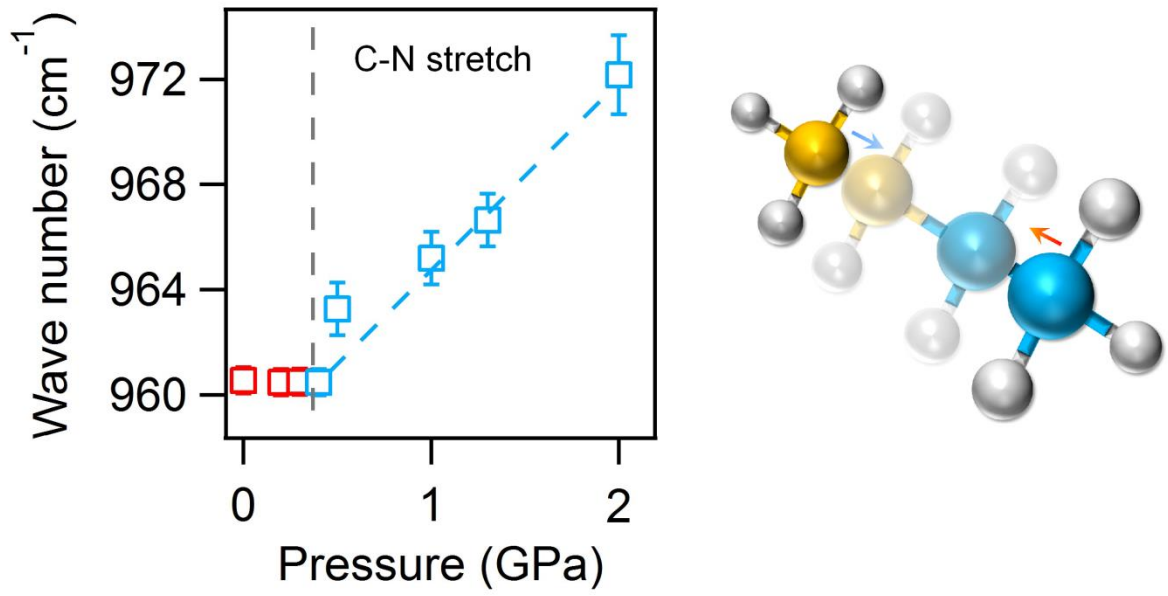

Figure S18. Pressure dependence of mid-IR C-N stretch mode. For all four modes, pressure-driven IR peak shifts are distinct between low pressure and high pressure phase ranges. Red and blue open squares represent the peak positions of the IR modes measured in a low pressure range corresponding to the *I4/mcm* phase and in a high pressure range corresponding to the *Imm2* phase, respectively. Grey dash lines indicate the approximate phase boundaries. Blue dash line is the guide to the eyes for blue-shift in the IR mode. Errors are derived from the function fitting of IR absorption peaks.

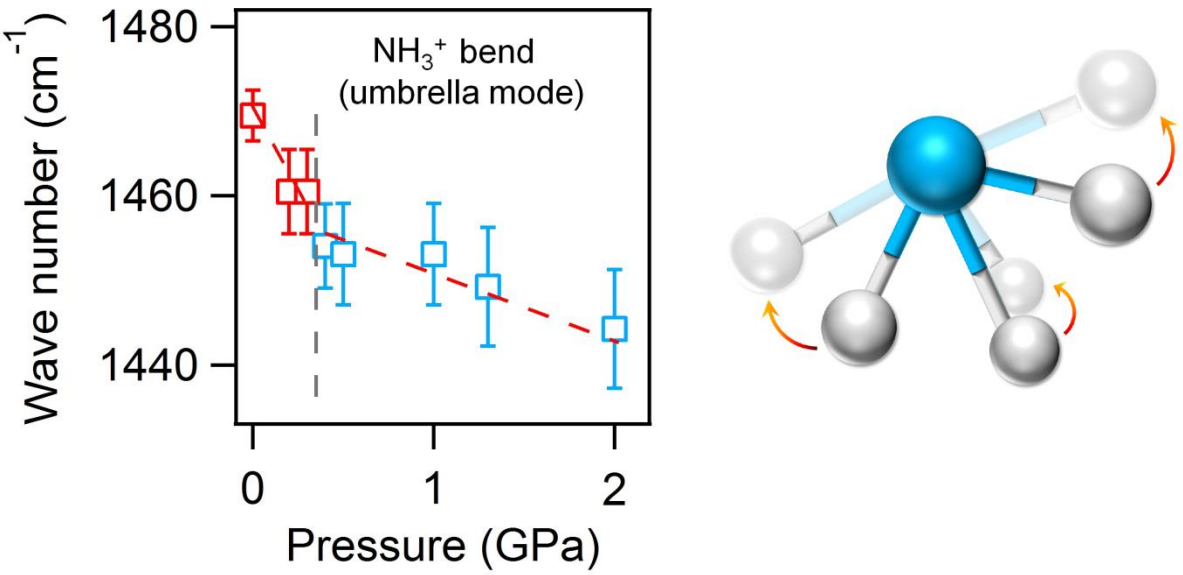

Figure S19. Pressure dependence of mid-IR NH_3^+ bend mode. Pressure-driven IR peak shifts are distinct between low pressure and high pressure phase ranges. Red and blue open squares represent the peak positions of the IR modes measured in a low pressure range corresponding to the *I4/mcm* phase and in a high pressure range corresponding to the *Imm2* phase, respectively. Grey dash lines indicate the approximate phase boundaries. Red dash lines are guides to the eyes for red-shifts in the IR mode. Errors are derived from the function fitting of IR absorption peaks.

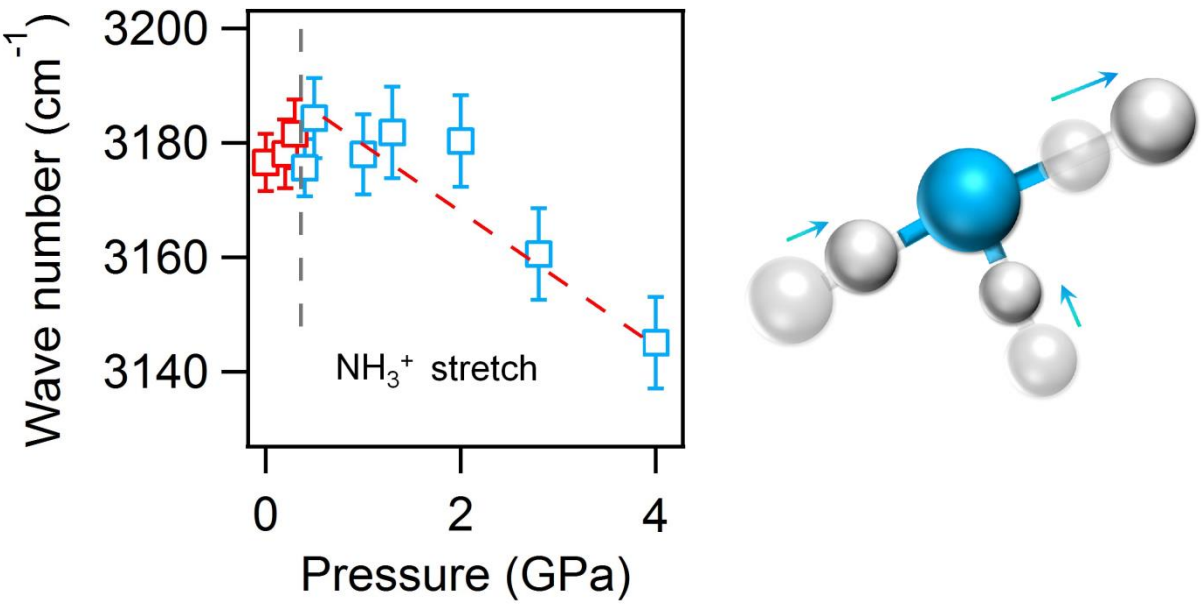

Figure S20. Pressure dependence of mid-IR NH_3^+ stretch modes. Pessure-driven IR peak shifts are distinct between low pressure and high pressure phase ranges. Red and blue open squares represent the peak positions of the IR modes measured in a low pressure range corresponding to the *I4/mcm* phase and in a high pressure range corresponding to the *Imm2* phase, respectively. Grey dash lines indicate the approximate phase boundaries. Red dash line is the guide to the eyes for red-shift in the IR modes. Errors are derived from the function fitting of IR absorption peaks.

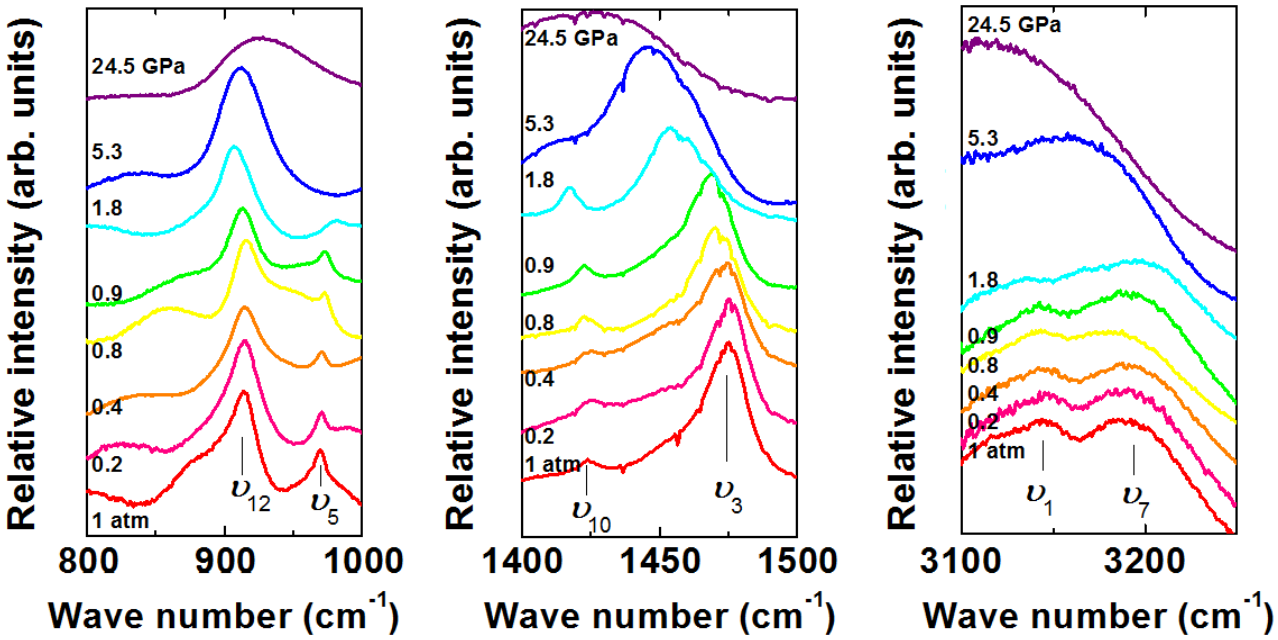

Figure S21. Pressure dependent mid-infrared spectra of $CH_3NH_3PbBr_3$ up to 24.5 GPa. Under ambient pressure, C-N stretch (ν_5) has a frequency at around 969 cm^{-1}, asymmetric CH_3 bending (ν_{10}) at around 1424 cm^{-1}, symmetric NH_3^+ bending (ν_3) at about 1475 cm^{-1}, asymmetric NH_3^+ stretching (ν_7) at about 3193 cm^{-1}, CH_3-NH_3^+ rock (ν_{12}) at around 915 cm^{-1}, and symmetric NH_3^+ stretching (ν_1) at around 3145 cm^{-1}. These assignments agree well with the reported values (7-10). Numbering ν_x of the peaks corresponds to the one given in ref. 7.

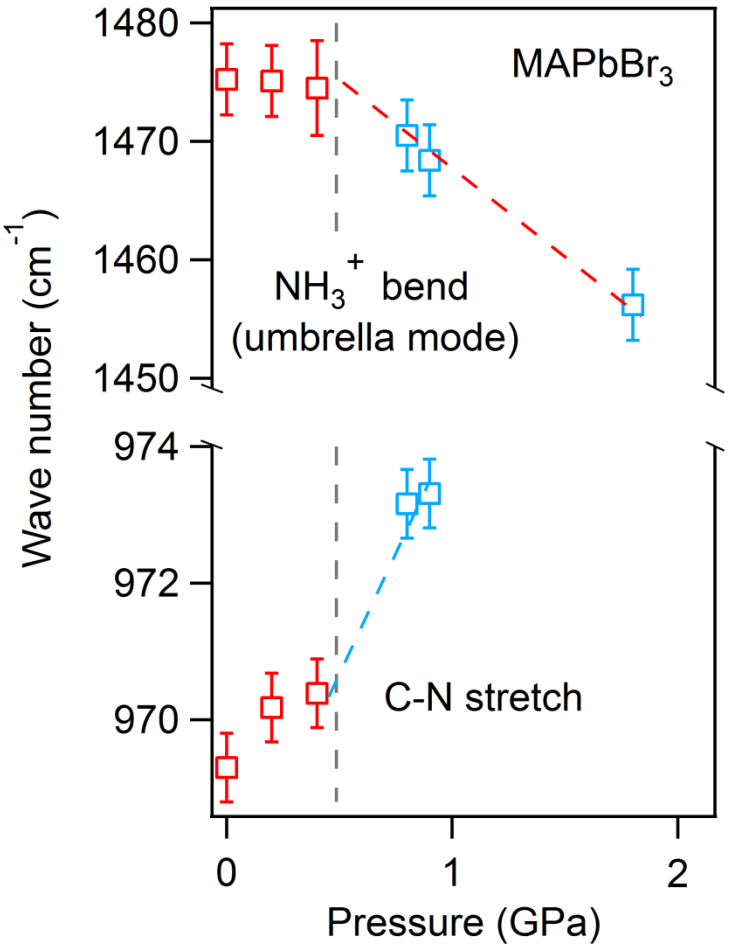

Figure S22. Pressure dependence of mid-IR NH_3^+ bend and C-N stretch modes, in which red-shift and blue-shift were observed, respectively, also similar to the tendencies observed in $MAPbI_3$. Red and blue open squares represent the peak positions of IR modes measured in a low pressure range corresponding to the $Pm\bar{3}m$ phase and in a high pressure range corresponding to the $Im\bar{3}$ phase, respectively. Blue and red dash lines serve as guides to the eyes for the blue-shifts and red-shifts in IR modes, respectively. Errors are derived from the function fitting of IR absorption peaks.

SI Section 5. High pressure optical absorption spectroscopy.

5.1 Band gap determination via Tauc plots.

Optical absorption measurements have been conducted as a function of pressure for $MAPbBr_3$, $MAPbI_3$, and $MA_2Pb(SCN)_2I_2$ samples. At each pressure point, a reference transmission spectrum was collected using the KBr sample before measuring transmission and the KBr spectra were used to determine a baseline. Fig. S23 shows the transmission spectra as a function of energy for the KBr ($I_0(E)$) and $MAPbI_3$ sample ($I_S(E)$) at an ambient pressure condition (both KBr and sample are loaded in an open DAC without applying any pressure). Then, the absorbance of $MAPbI_3$ sample can be obtained by (11)

$$\alpha(E)d = -\ln(T(E)) = -\ln(I_S(E) / I_0(E)) . \quad \text{(S-1)}$$

Here, α is absorbance coefficient and d is the sample thickness. $T(E)$ is the transmittance as a function of energy. Based on the transmission spectra of the KBr and $MAPbI_3$ sample (see Fig. S23), the absorbance of the $MAPbI_3$ sample at ambient pressure was obtained and the result is shown in Fig. S24. The nature of the band gap can be estimated by examining Tauc plots as (12-14)

$$(\alpha dhv)^2 \propto hv \quad \text{(S-2)}$$

and

$$(\alpha dhv)^{1/2} \propto hv \quad \text{(S-3)}$$

for direct and indirect band gap, respectively. Then, the magnitude of band gap, Eg, can be given by extrapolating the linear portion of the Tauc plot to the baseline. Better linear fits were obtained for the direct band gap Tauc plots for both $MAPbBr_3$ and $MAPbI_3$. In addition, the direct band gap nature is also further supported by our theoretical calculations (see Section 6 for details). Therefore, the Eg values derived from fittings for direct band gap were used.

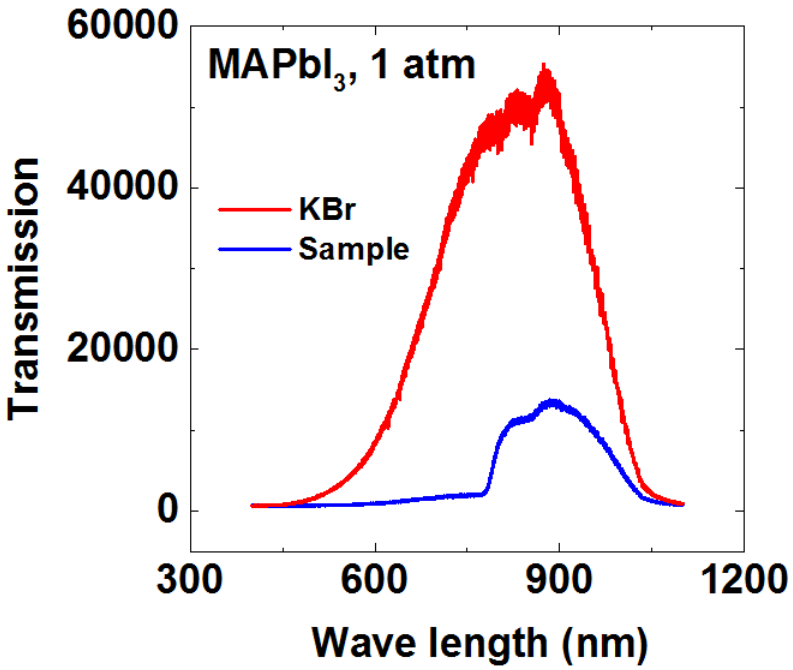

Figure S23. Transmission spectra of KBr and $MAPbI_3$ sample at ambient pressure.

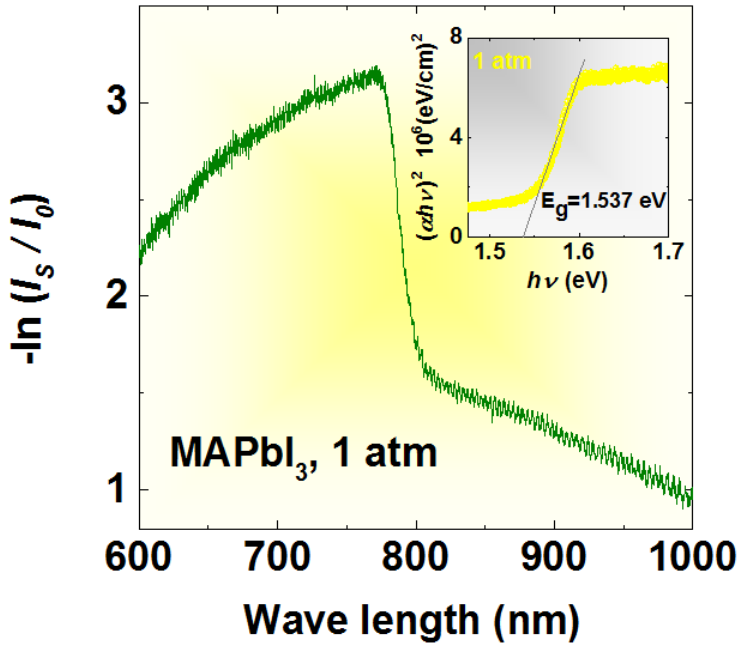

Figure S24. Absorbance spectra of the $MAPbI_3$ sample at ambient pressure. Inset shows the Tauc plot fitting result using direct band gap model. The linear extrapolation used to determine

Eg is shown with a grey line. Note that the sample thickness *d* here is around ~20 μm. Similar extrapolations were made in Figs. S25-S26. It should be pointed out that the thickness of sample *d* does not vary significantly as a function of pressure at a mild range. In addition, *d* is not energy dependent and the changing in *d* will not affect the fitting result for the Tauc plots.

5.2 Band gap-pressure relationship determination for $MAPbBr_3$.

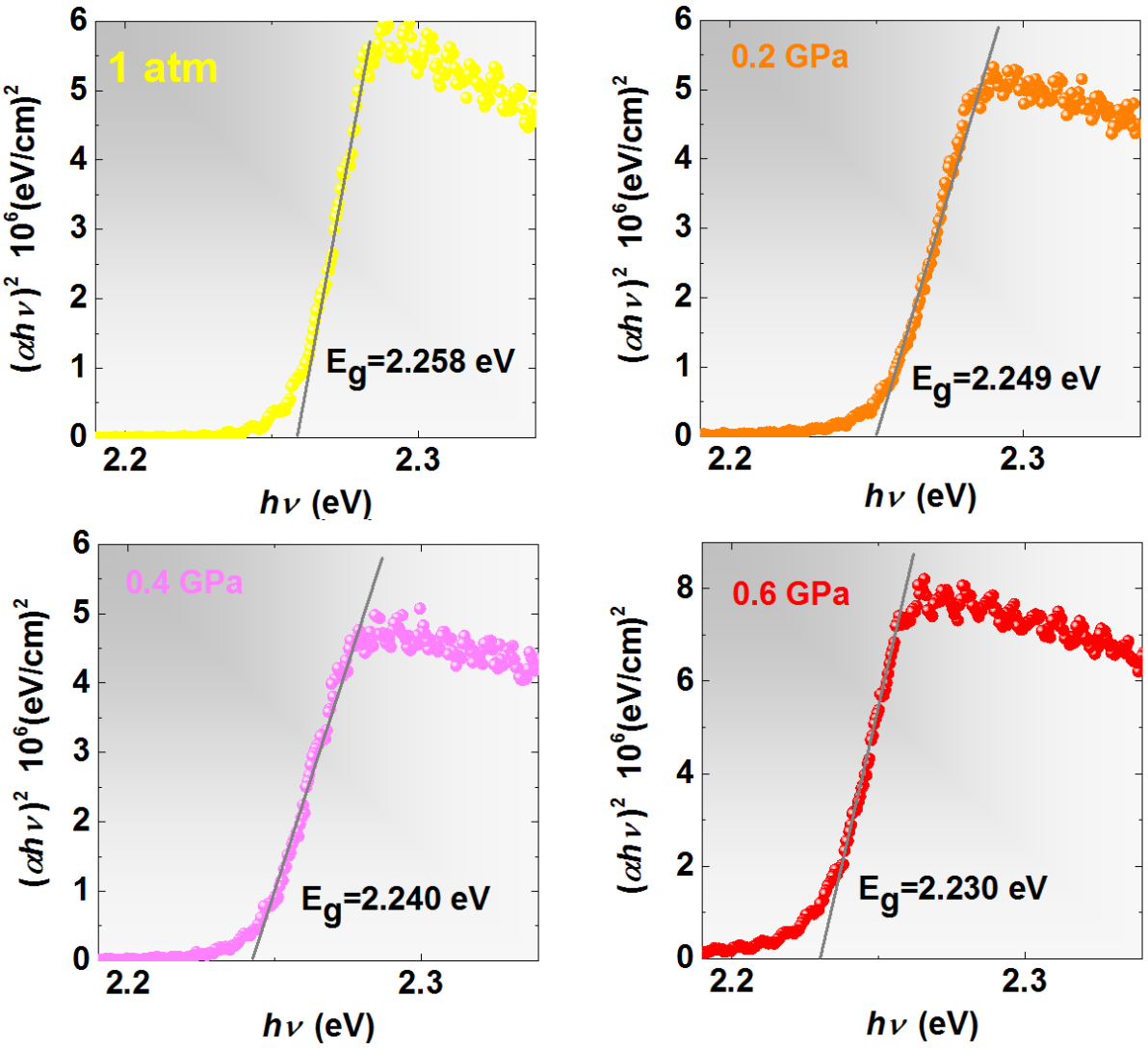

Figure S25. Direct band gap Tauc plots for $MAPbBr_3$ at an ambient condition, 0.2 GPa, 0.4 GPa, and 0.6 GPa (in compression). Red-shift was observed from 2.258 eV at 1 atm down to 2.230 eV at 0.6 GPa.

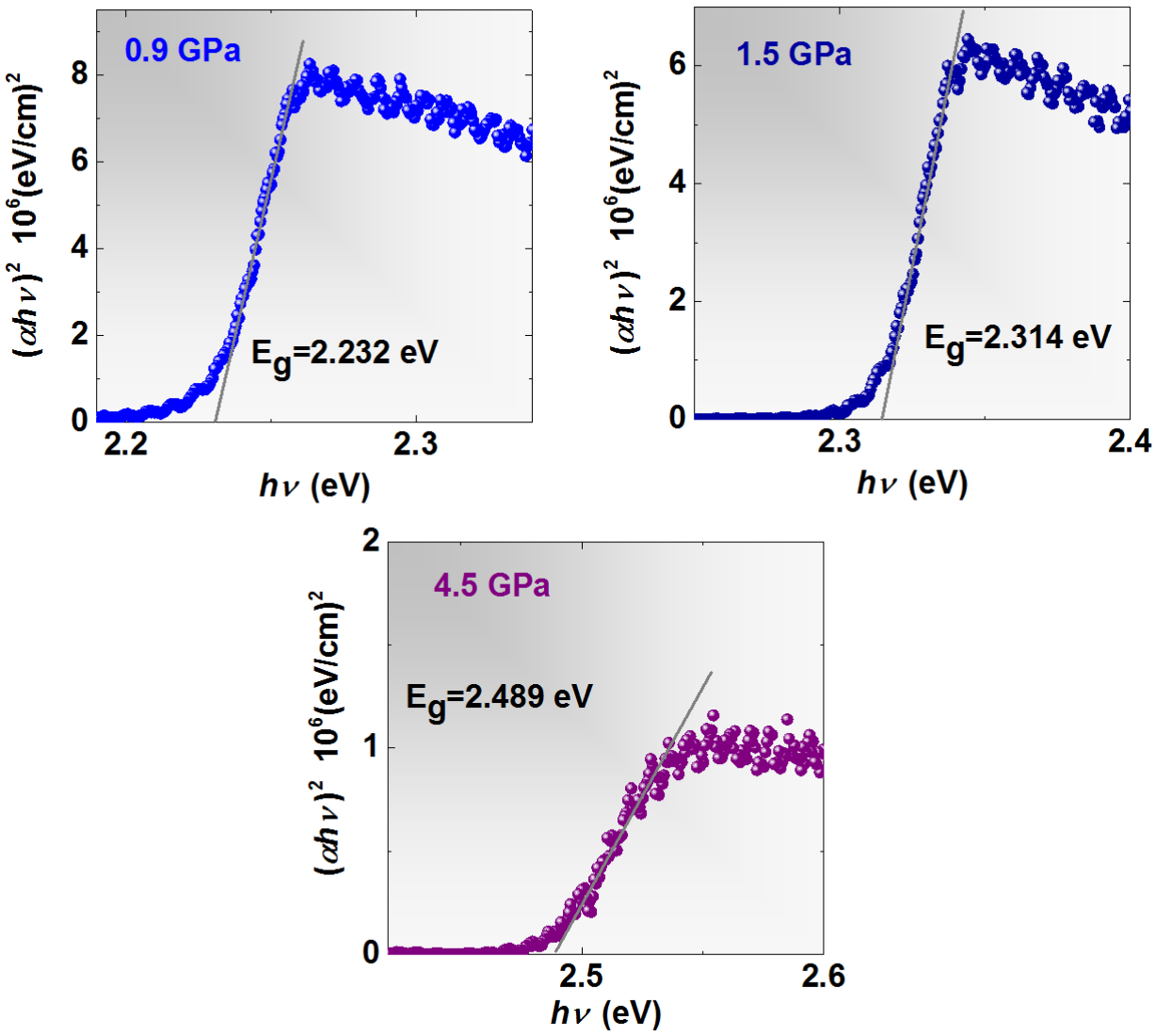

Figure S26. Direct band gap Tauc plots for $MAPbBr_3$ at 0.9 GPa, 1.5 GPa, and 4.5 GPa (in compression). Blue-shift was observed from 2.232 eV at 0.9 GPa up to 2.489 eV at 4.5 GPa.

SI Section 6. First-principles computer simulations.

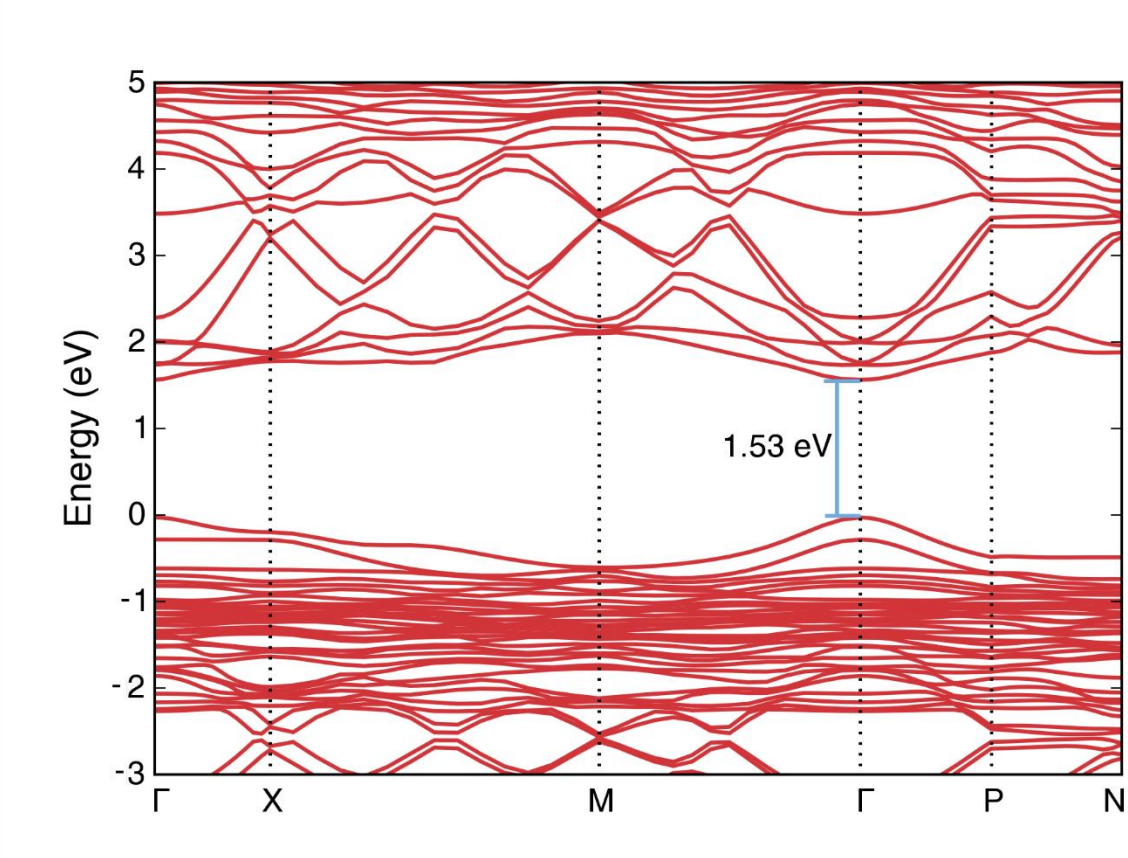

Figure S27. Calculated electronic band structure of $MAPbI_3$ at an ambient condition. Structural parameters used for calculation are derived from our single crystal diffraction data. A direct band gap of 1.53 eV was observed, as shown in this figure.

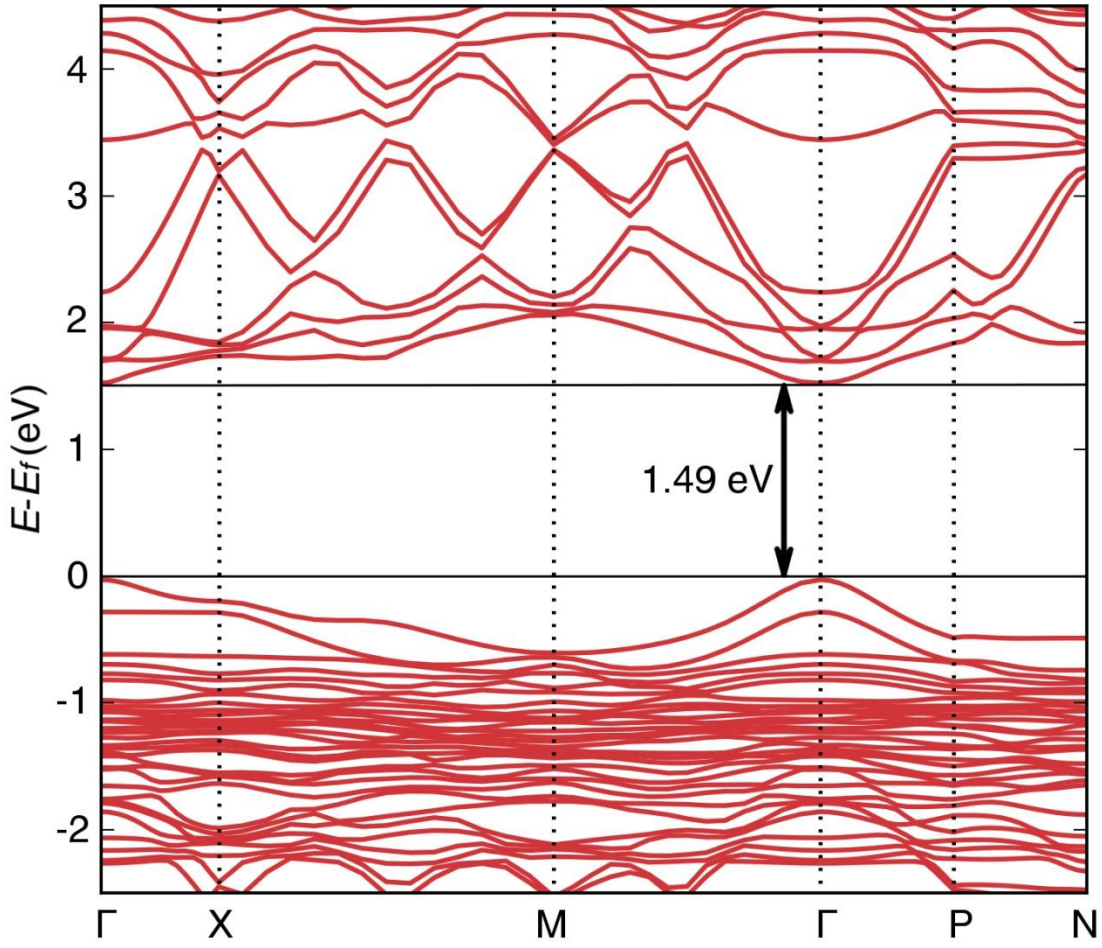

Figure S28. Calculated electronic band structure of $MAPbI_3$ at 0.4 GPa using space group *I4/mcm* as structural model. Data from our single crystal experiments are used as initial crystal structures and then the structural parameters at 0.4 GPa used for calculation can be obtained from the optmized method in which the Quasi-Newton steps is lower than 10^{-6} eV and the forces acting on each atom are less than 0.02 eV $Å^{-1}$. Direct band gap of 1.49 eV was observed, as shown in this figure.

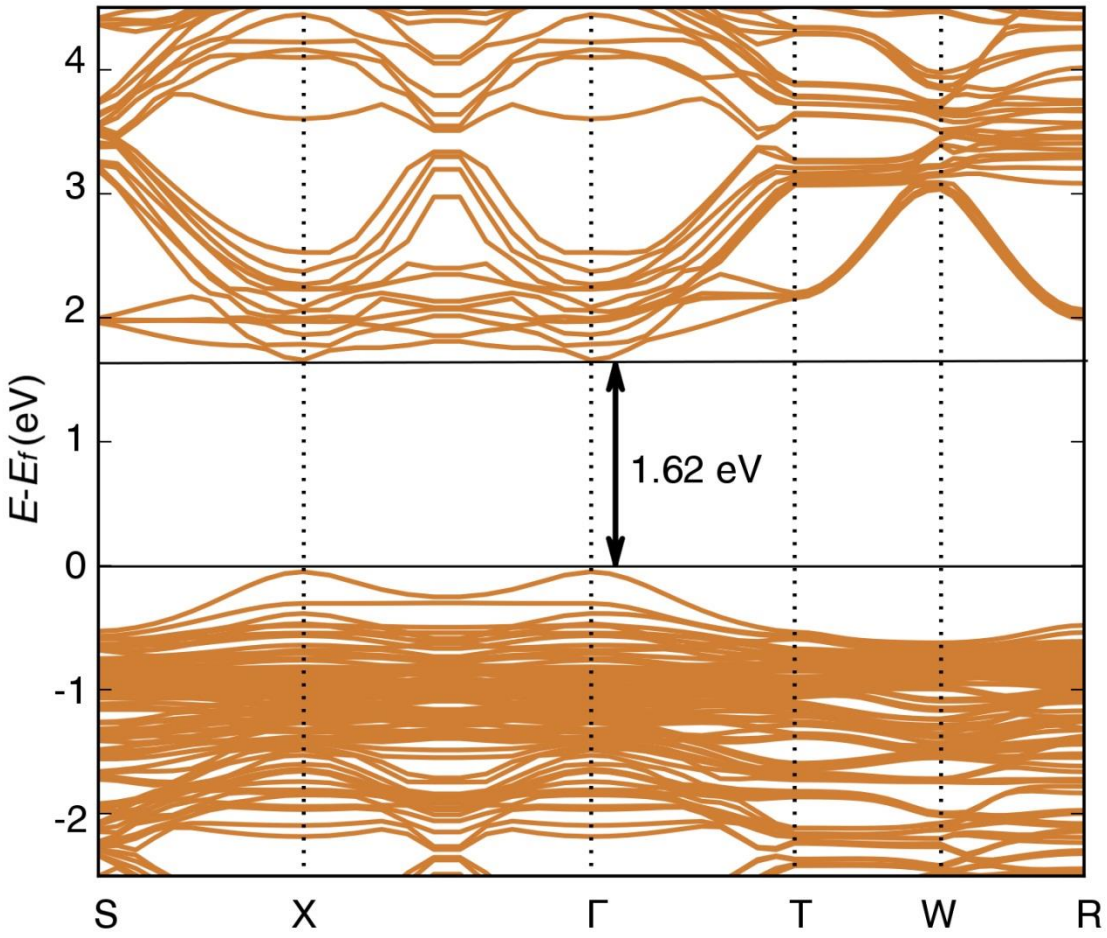

Figure S29. Calculated electronic band structure of $MAPbI_3$ at 0.4 GPa using the space group *Imm2* as a structural model. Structural parameters used for the calculation are derived from our single crystal diffraction data. A direct band gap of 1.62 eV was observed, as shown in this figure.

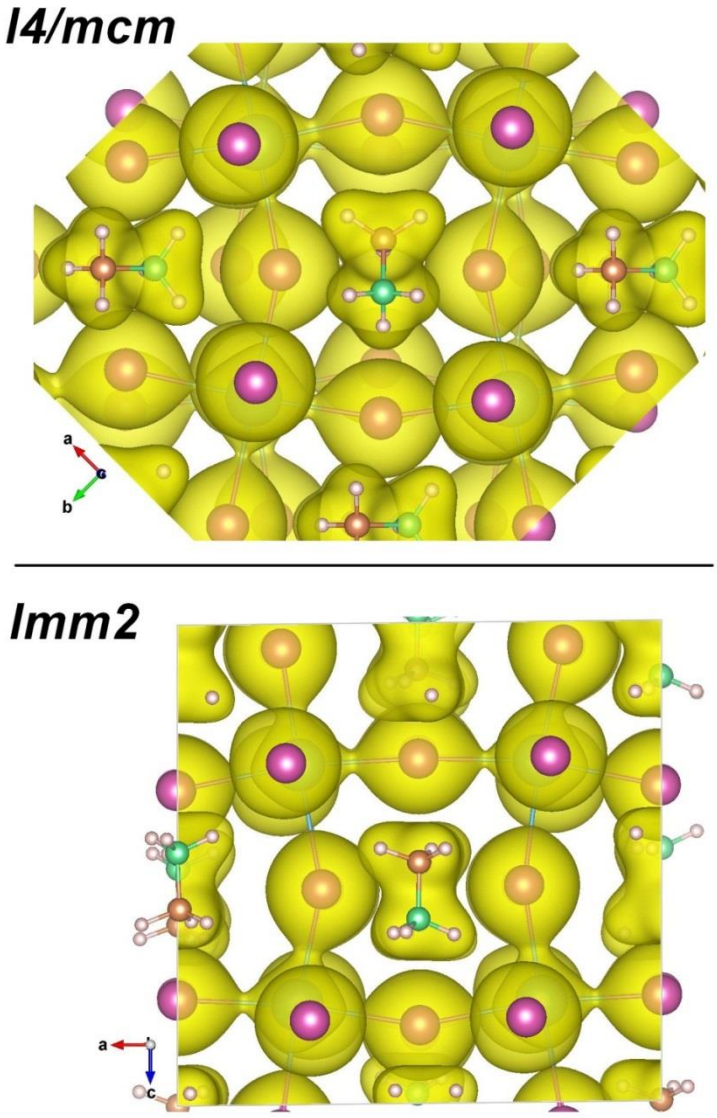

Figure S30. Charge density of $MAPbI_3$ with *I4/mcm* (up) and *Imm2* (down) structures. Charge redistribution was demonstrated due to the titling of the Pb-I octahedral as the pressure-driven phase transition of *I4/mcm* to *Imm2* occurs. Compared to the low pressure phase *I4/mcm*, the high pressure phase *Imm2* has less electronic charge density overlapping between the Pb and I atoms. Symbols: purple spheres: I atoms, brown spheres: C atoms, green spheres: N atoms, and white spheres: H atoms. Pb atoms are hidden in the shadow.

SI Section 7. High pressure carrier lifetime measurements

7.1 Biexponential decay

All PL decay traces obtained in this work can be fitted well using a biexponential decay function as follows (15),

$$I_{\mathrm{PL}}(t) = I_{\mathrm{int}}[\alpha \cdot \exp(-t/\tau_1) + \beta \cdot \exp(-t/\tau_2) + I_0] \quad \text{(S-4)}$$

where $I_{PL}(t)$ is the time dependent PL intensity; I_{int} is the initial PL intensity; I_0 is the background constant (nearly to zero for all measurements in this work); t is time; τ_1 and τ_2 are the characteristic lifetime of slow and fast components derived from fitting results, and α and β are pre-exponential factors coefficients for τ_1 and τ_2, respectively. The values of α and β factors can give information about the contribution from slow or fast components of carrier lifetime to the average one. Using the characteristic lifetime and pre-exponential factors values for both slow and fast components, we obtain the average lifetime, $<\tau>$, using the following relationship:

$$<\tau> = \frac{\sum \alpha_i \tau_i^2}{\sum \alpha_i \tau_i} = \frac{\alpha\tau_1^2 + \beta\tau_2^2}{\alpha\tau_1 + \beta\tau_2} \quad \text{(S-5)}$$

Eq. (S-5) considers the relative contribution of the two terms of τ_1 and τ_2 to the static PL evaluated by integrating the respective exponential traces. From Eq. (S-5) one can see that a long average carrier lifetime can be readily obtained if the slow part τ_1 made a dominated contribution, namely, a large α/β value. τ_1 and τ_2 are assigned to the presence of a surface component (fast part, τ_2) together with a bulk component (slow part, τ_1) (14). Thus, a long average carrier lifetime suggests the lifetime of carriers propagating deeper in the material. PL time decay trace on $MAPbI_3$ and $MAPbBr_3$ at various pressures in the compression process are shown in Figs. S31-S36, and Figs. S37-S43, respectively. The fitted results for measured decay traces of three samples are listed in Tables. S7-S8, respectively.

7.2 Observed trace decay and carrier lifetime for $MAPbI_3$

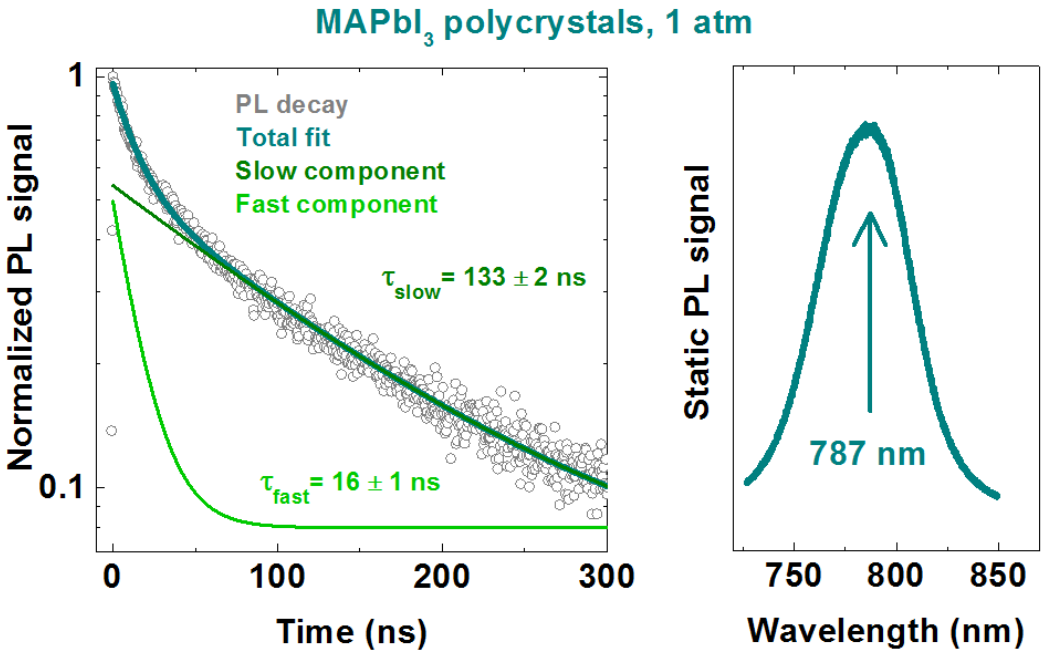

Figure S31. PL decay trace of $MAPbI_3$ polycrystals at ambient pressure with static photoluminescence at 787 nm.

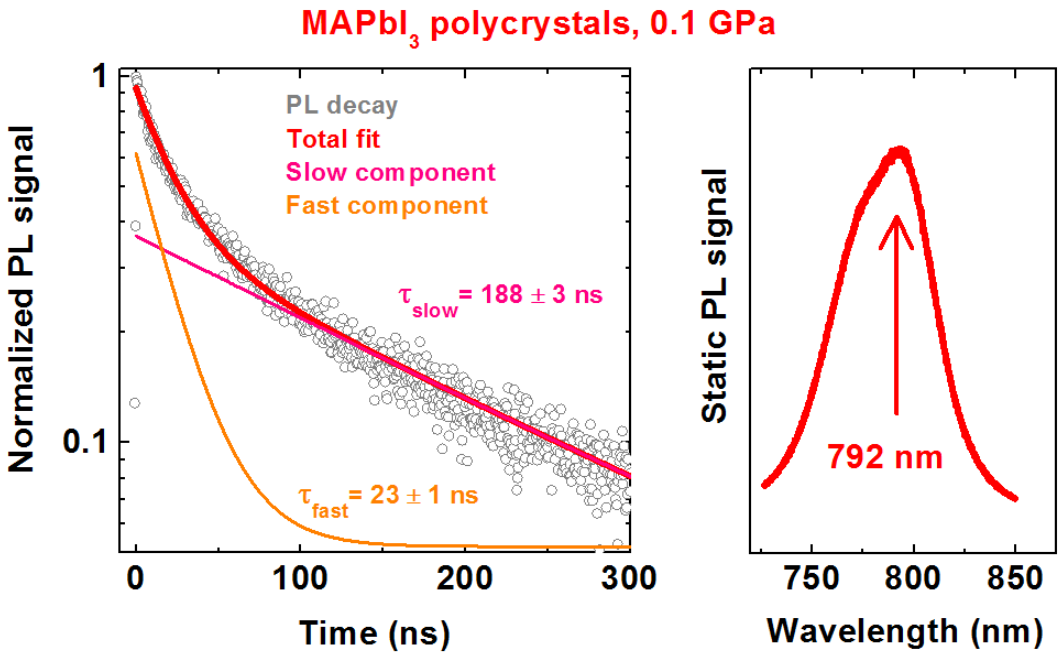

Figure S32. PL decay trace of $MAPbI_3$ polycrystals at 0.1 GPa with static photoluminescence at 792 nm.

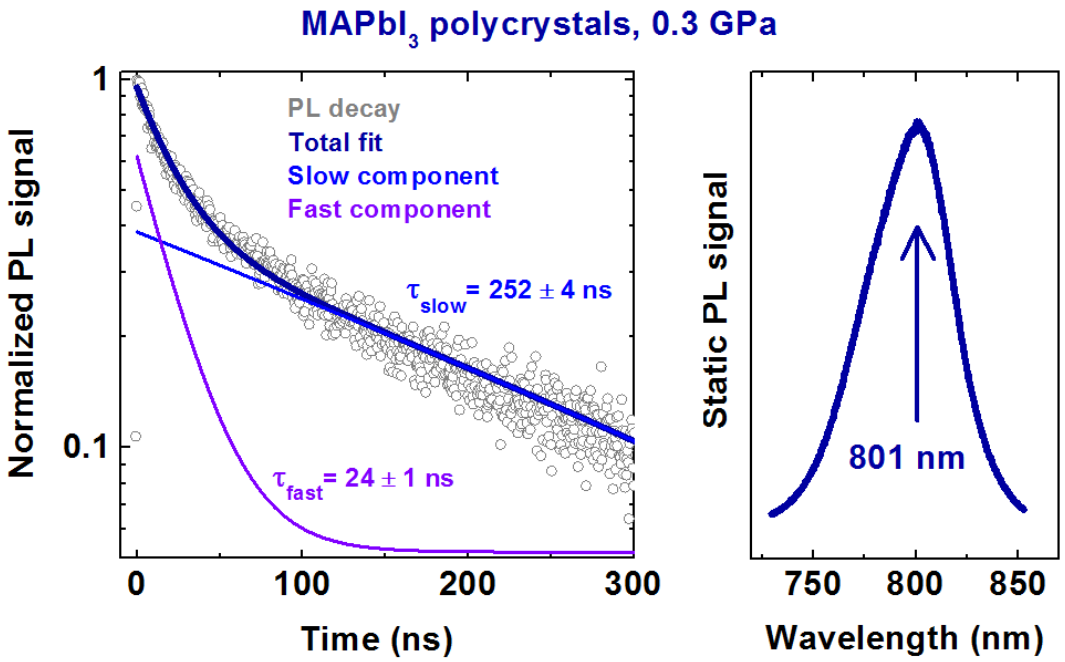

Figure S33. PL decay trace of $MAPbI_3$ polycrystals at 0.3 GPa with static photoluminescence at 801 nm.

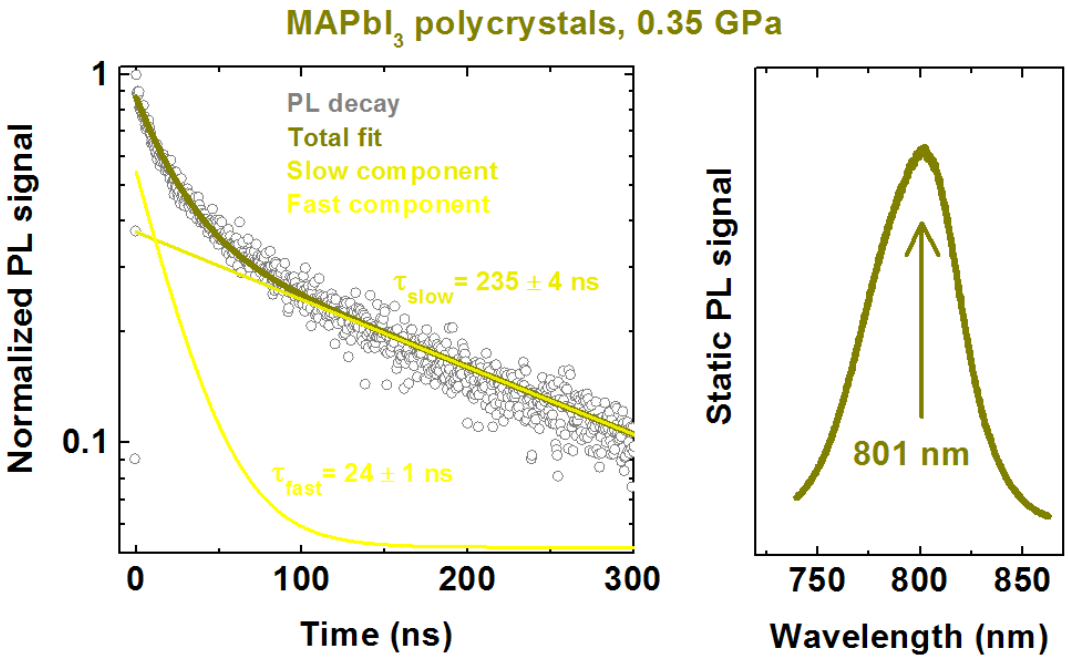

Figure S34. PL decay trace of $MAPbI_3$ polycrystals at 0.35 GPa with static photoluminescence at 801 nm.

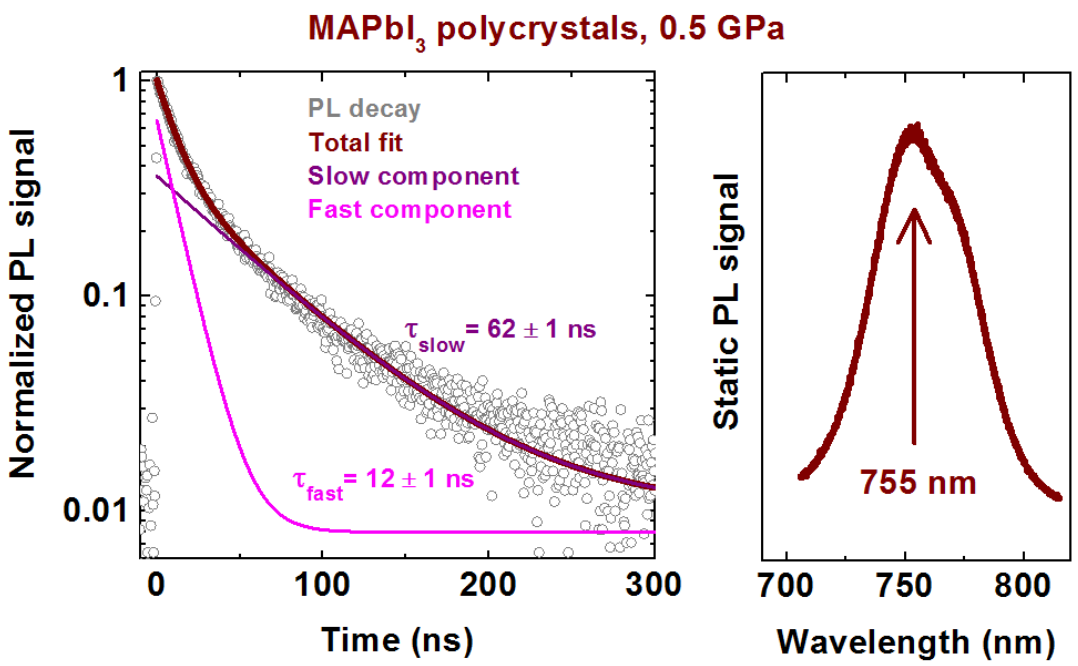

Figure S35. PL decay trace of $MAPbI_3$ polycrystals at 0.5 GPa with static photoluminescence at 755 nm.

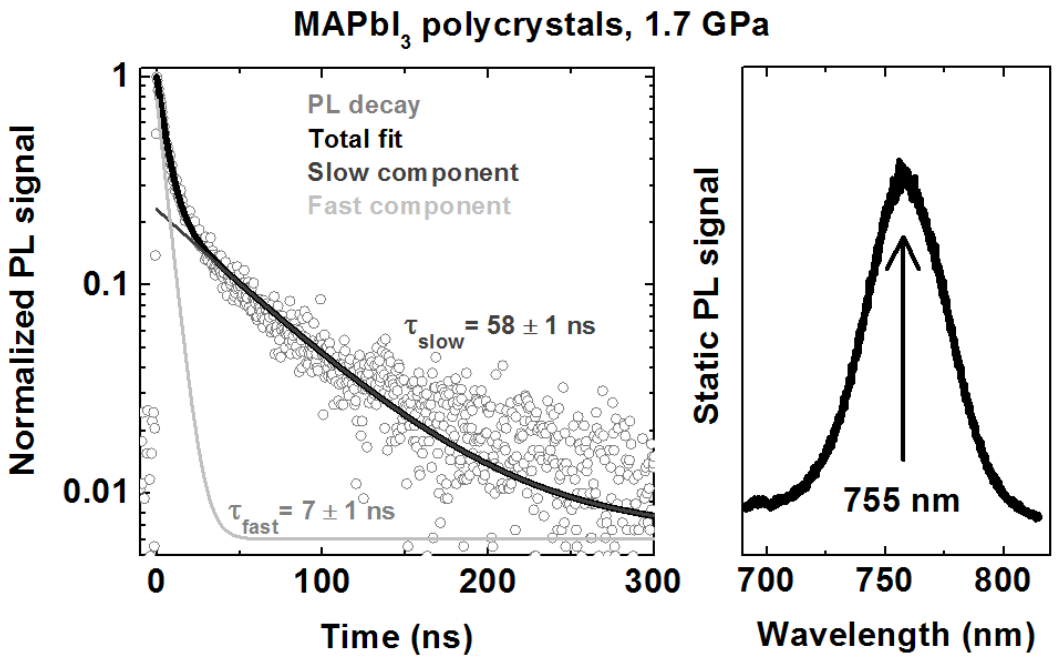

Figure S36. PL decay trace of $MAPbI_3$ polycrystals at 1.7 GPa with static photoluminescence at 755 nm.

Table S7. Time constants for the biexponential decay observed in the PL dynamics for the first 500 ps following photoexcitation of $MAPbI_3$ polycrystals as a function of pressure (Fitting function: $I_{PL}(t) = I_{int}[\alpha \cdot \exp(-t/\tau_1) + \beta \cdot \exp(-t/\tau_2) + I_0]$).

Pressure	α	β	τ_1 †	τ_2 †	$<\tau>$ ‡
1 atm	0.36875	0.62735	133 ±2 ns	16 ±1 ns	114.00 ns
0.1 GPa	0.35909	0.56390	188 ±3 ns	23 ±1 ns	161.41 ns
0.3 GPa	0.40511	0.56637	252 ±4 ns	24 ±1 ns	225.21 ns
0.35 GPa	0.37213	0.49254	235 ±4 ns	24 ±1 ns	209.87 ns
0.5 GPa	0.35135	0.64568	62 ±1 ns	12 ±1 ns	48.88 ns
1.7 GPa	0.22417	0.76833	58 ±1 ns	7 ±1 ns	43.07 ns

†Errors are derived from the fitting function.

‡$<\tau>$ represents the mean lifetime, which can be calculated by $<\tau> = \frac{\alpha\tau_1^2 + \beta\tau_2^2}{\alpha\tau_1 + \beta\tau_2}$.

7.3 Observed trace decay and carrier lifetime for $MAPbBr_3$

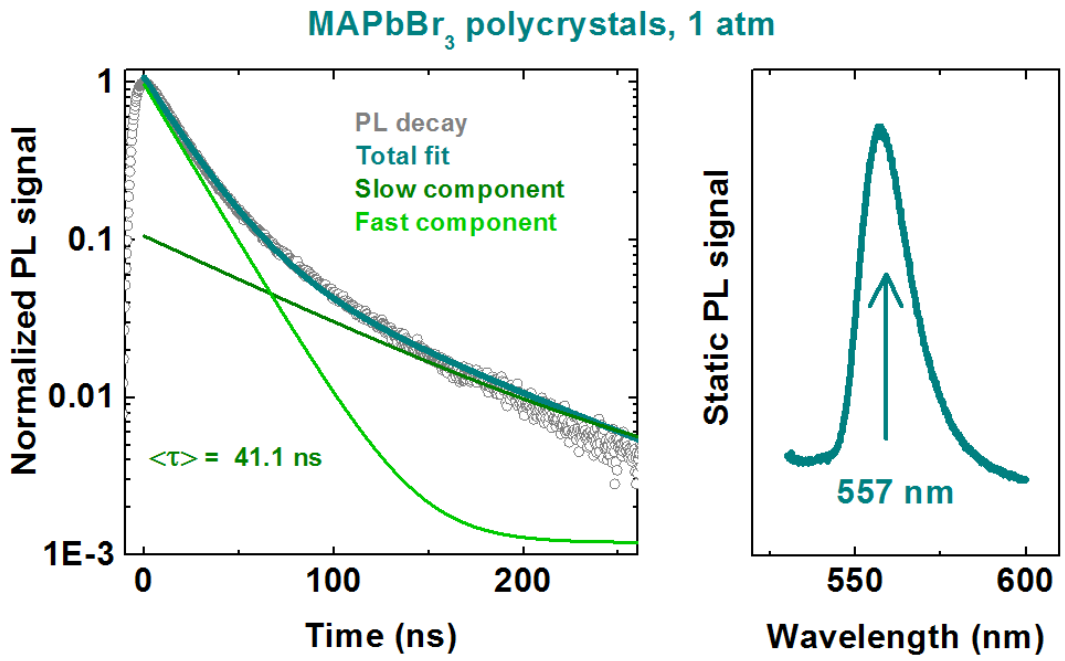

Figure S37. PL decay trace of $MAPbBr_3$ polycrystals at ambient pressure with static photoluminescence at 557 nm.

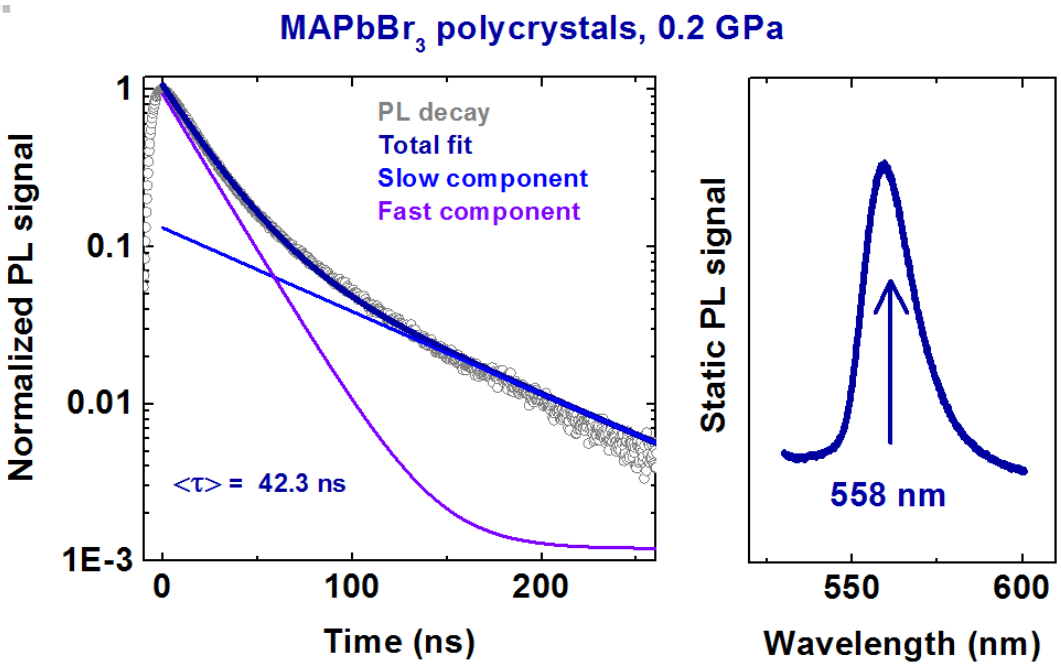

Figure S38. PL decay trace of $MAPbBr_3$ polycrystals at 0.2 GPa with static photoluminescence at 558 nm.

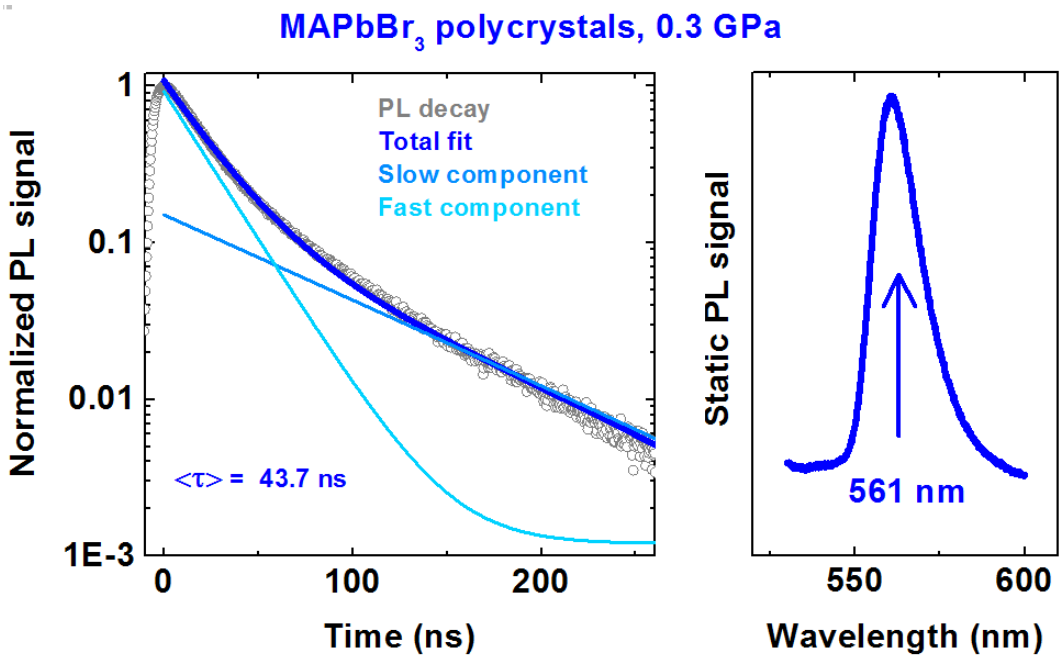

Figure S39. PL decay trace of $MAPbBr_3$ polycrystals at 0.3 GPa with static photoluminescence at 561 nm.

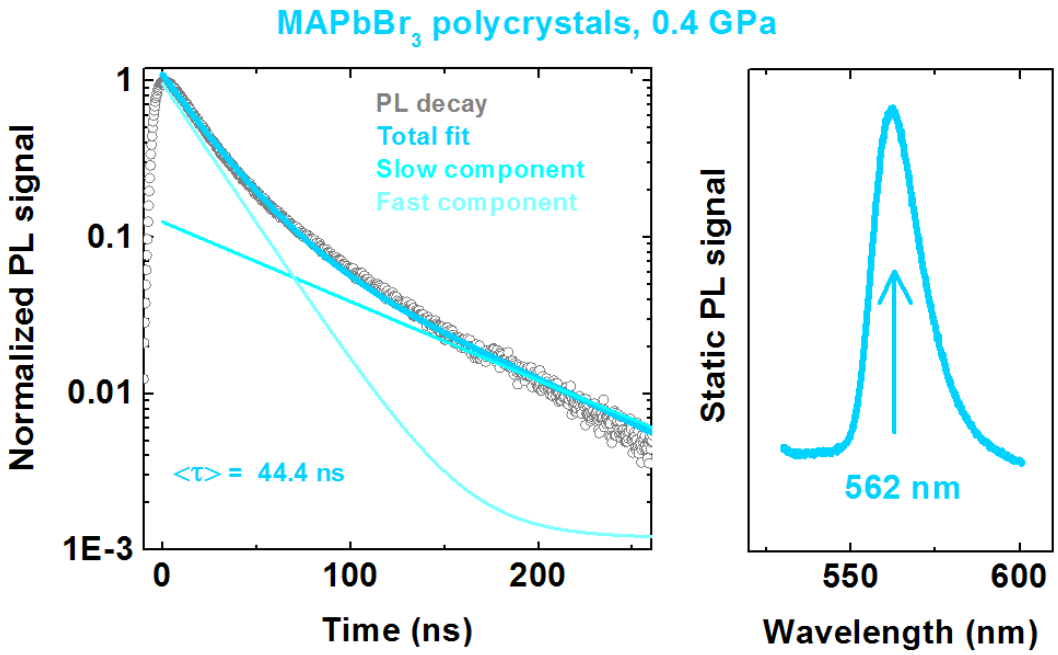

Figure S40. PL decay trace of $MAPbBr_3$ polycrystals at 0.4 GPa with static photoluminescence at 562 nm.

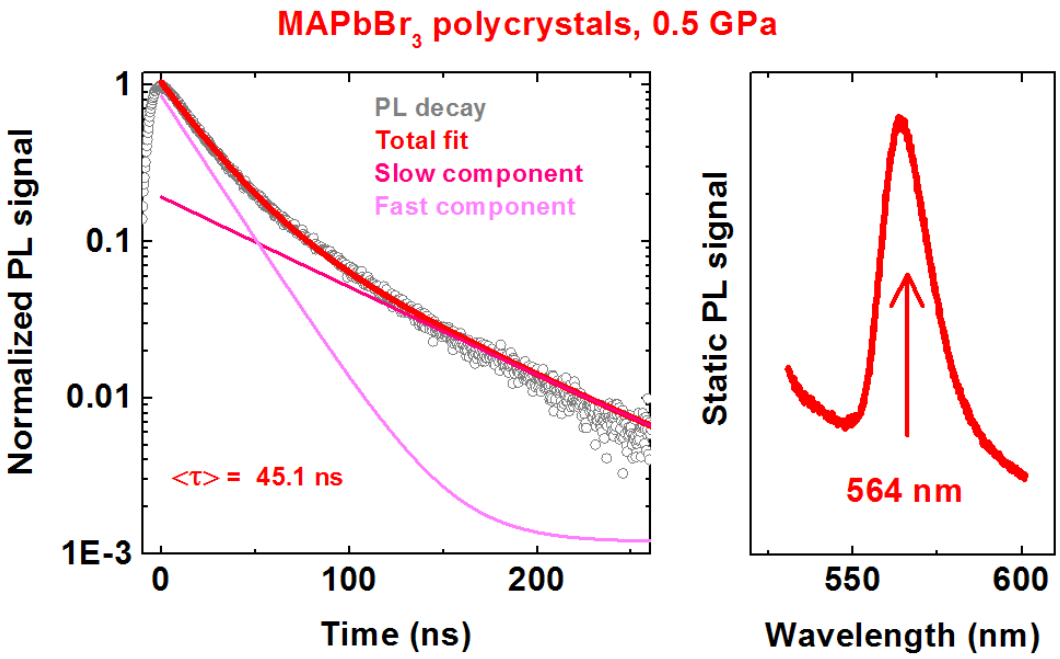

Figure S41. PL decay trace of $MAPbBr_3$ polycrystals at 0.5 GPa with static photoluminescence at 564 nm.

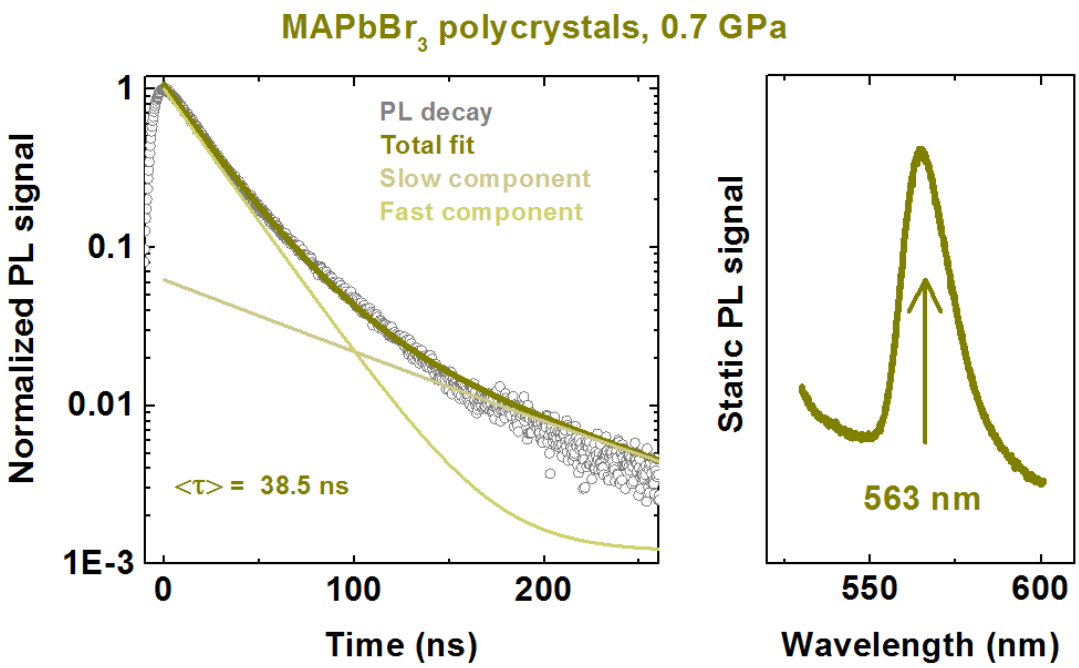

Figure S42. PL decay trace of $MAPbBr_3$ polycrystals at 0.7 GPa with static photoluminescence at 563 nm.

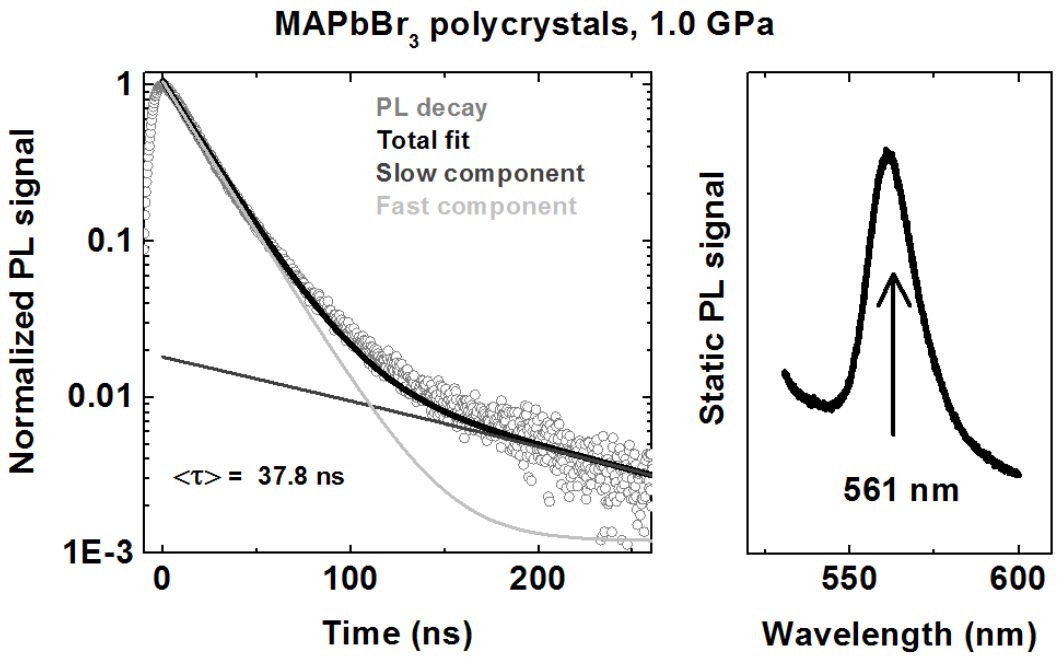

Figure S43. PL decay trace of $MAPbBr_3$ polycrystals at 1.0 GPa with static photoluminescence at 561 nm.

Table S8. Time constants for the biexponential decay observed in the PL dynamics for the first 300 ps following photoexcitation of $MAPbBr_3$ polycrystals as a function of pressure (Fitting function: $I_{PL}(t) = I_{int}[\alpha \cdot \exp(-t/\tau_1) + \beta \cdot \exp(-t/\tau_2) + I_0]$).

Pressure	α	β	τ_1 †	τ_2 †	$<\tau>$ ‡
1 atm	0.10381	0.96989	87 ±3 ns	22 ±1 ns	41.08 ns
0.2 GPa	0.13152	0.93091	81 ±2 ns	22 ±1 ns	42.28 ns
0.3 GPa	0.15074	0.92635	80 ±1 ns	23 ±1 ns	43.67 ns
0.4 GPa	0.13591	0.95884	85 ±1 ns	24 ±1 ns	44.37 ns
0.5 GPa	0.19173	0.84855	74 ±1 ns	24 ±1 ns	45.05 ns
0.7 GPa	0.06181	0.99917	94 ±2 ns	26 ±1 ns	38.48 ns
1.0 GPa	0.01859	1.05351	160 ±5 ns	22 ±1 ns	37.83 ns

†Errors are derived from the fitting function.

‡$<\tau>$ represents the mean lifetime, which can be calculated by $<\tau> = \frac{\alpha\tau_1^2 + \beta\tau_2^2}{\alpha\tau_1 + \beta\tau_2}$.

7.5 The role of pre-exponential factors in average carrier lifetime

The ratio of pre-exponential factors for the slow and fast part of lifetime, α/β, play an important role in the final average lifetime: Short average carrier lifetime in some cases is not weird if small α/β values can be demonstrated, even if the fitted slow component of carrier lifetime is long. Fig. S44 give the α/β values for $MAPbBr_3$ polycrystals at various pressures, from which one can see that at relatively high pressures, such as at 1.0 GPa, the α/β values are much lower than those at lower pressure, and lead to a final shorter average carrier lifetime.

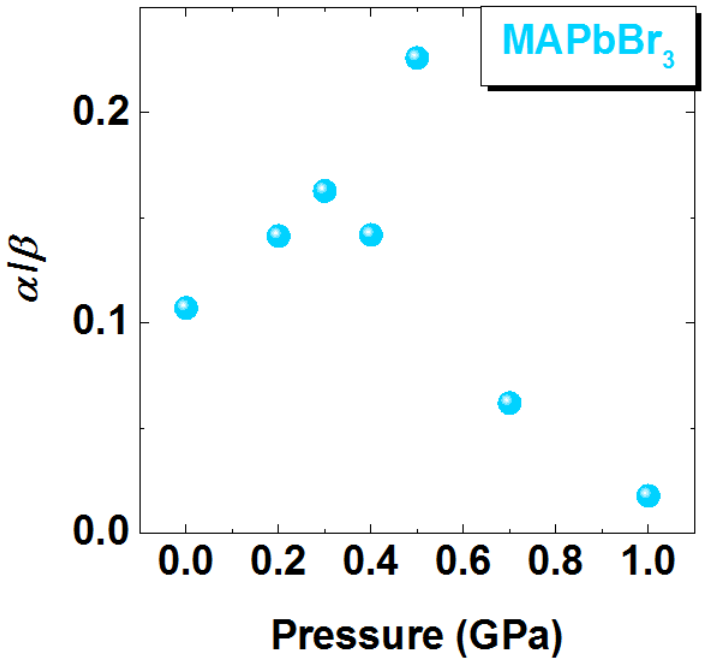

Figure S44. The ratio of pre-exponential factors, α/β, for $MAPbBr_3$ polycrystals as a function of pressure in compression up to 1.0 GPa.

SI Materials and methods

1. Materials.

1.1. Chemicals.

γ-Butyrolactone (≥99%), sodium thiocyanate (98%), hydroiodic acid (57 wt. % in H_2O), methylamine solution (40 wt.% in H_2O) and tetrahydrofuran (anhydrous, ≥99.9%) were purchased from Aldrich. Lead(II) iodide (99.9985% metals basis), N, N-dimethylformamide (99.8%, packaged under Argon) and lead(II) tetrafluoroborate (50 wt. % in H_2O) were purchased from Alfa Aesar. Lead nitrate was purchased from Mallinckrodt. Hydrobromic acid standard solution (1.997 mol/L) was purchased from Fluka. Hexanes (99.9%) and ethyl ether (anhydrous) was purchased from Fischer Chemicals. All chemicals were directly used as received without further treatments.

1.2. Precursors.

Methylammonium iodide (CH_3NH_3I, MAI) was synthesized by using the method reported in literature (16) with slight modifications. In detail, 24 mL of 40% CH_3NH_2 aqueous solution was dropwise introduced into 10 mL HI aqueous solution for reaction in a 250 mL round bottom flask immersed in ice bath under ambient conditions, accompanied by constant stirring. This mixture solution was then allowed to fully react for 2 hours with stirring. Pure MAI was obtained by extracting the solvent in a rotary evaporator at 60 ˚C, followed by ethyl ether washing, vacuum filtration on filter paper and drying at 90 ˚C overnight in a vacuum oven. Methylammonium bromide (CH_3NH_3Br, MABr) was synthesized in a similar fashion. Equimolar of CH_3NH_2 was slowly added to HBr in a 250 mL round bottom flask immersed in an ice bath. The mixture of compounds was stirred for 60 minutes. Pure MABr was obtained by rotary evaporation at 60 ˚C. Lead(II) bromide ($PbBr_2$) was made by 1:2 molar ratio of $Pb(NO_3)_2$

and HBr. The $PbBr_2$ precipitate was filtered out and then rinsed thoroughly with copious amounts of deionized water 3 times, followed by drying in a vacuum oven at 100 ˚C overnight.

1.3. Polycrystals preparation.

$MAPbI_3$ polycrystals

Methylammonium lead iodide ($CH_3NH_3PbI_3$, $MAPbI_3$) precursor solution was first made by dissolving 0.29 g PbI_2 and 0.1 g MAI in 0.52 mL γ-butyrolactone at 60 ˚C and stirring for 3 hours (17). This as-prepared solution was then hot-casted onto a cleaned glass slide at 110 ˚C. After the solvent evaporated, $MAPbI_3$ polycrystals were collected by carefully scraping down the glass slide using a plastic slide.

$MAPbBr_3$ polycrystals

Methylammonium lead bromide ($CH_3NH_3PbBr_3$, $MAPbBr_3$) precursor solution was first prepared by dissolving 0.23 g $PbBr_2$ and 0.1 g MAI in 0.52 mL dimethylformamide at 60 ˚C and stirring for 3 hours. The solution was hot-casted onto a cleaned glass slide at 110 ˚C. After the solvent evaporated, $MAPbI_3$ polycrystals were collected by carefully scraping down the glass slide.

1.4. Single crystals preparation.

$MAPbI_3$ single crystal

$MAPbI_3$ single crystals were grown by first reacting equimolar amounts of MAI with lead (II) iodide in γ-butyrolactone to form a 1 M solution of MAI/PbI_2. The resulting solution was then heated at 110 ˚C for 3 hours to precipitate small black seed crystals. A seed crystal was then transferred to a fresh 1 M MAI/PbI_2 solution to continue the crystal growth for 48 hours at 70 ˚C in darkness, without disturbance. Micrographs of the harvested $MAPbI_3$ crystals are shown in Fig. S3. The best samples were picked for further study.

2. Methods.

2.1. Synchrotron powder X-ray diffraction (XRD) at ambient conditions

The crystal structures of the polycrystalline samples at ambient conditions (room temperature, 1 atm) were determined using the high resolution synchrotron X-ray facility, 11-BM of the Advanced Photon Source (APS), Argonne National Laboratory (ANL). The instrument resolution is $\Delta d/d$ ~0.00017, using twelve silicon (111) crystal analyzers positioned in front of the $LaCl_3$ scintillation detectors, representing the state-of-the-art *d*-spacing resolution for diffraction measurements (18). Samples were tightly packed in a Krapton tube with a diameter of 0.3 mm and tightly sealed with wax. Diffraction patterns were measured using an X-ray wavelength of 0.414162 Å over the 2θ range of 4.0°–24.0°, with a 0.002° 2θ step-size. High quality experimental data were refined using GSAS program (19).

2.2. *In situ* synchrotron high pressure powder X-ray diffraction

In-situ synchrotron high pressure powder XRD experiments were carried out at the 13-BM-C of the Advanced Photon Source (APS), Argonne National Laboratory (ANL). A monochromatic X-ray with a wavelength of 0.434 Å was employed and the incident X-ray beam was focused to a 15 μm × 15 μm spot. XRD patterns were collected with a MAR165 CCD detector. The samples were loaded in a symmetric-type diamond anvil cell (DAC) with a pair of 400 μm culets and placed in a rhenium (Re) gasket hole with a diameter of 200 μm drilled by a laser micro-matching system (20). Silicon oil was used as pressure-transmitting medium. It should be noted that methanol/ethanol cannot be used as our organic-inorganic hybrid samples because they are easily decomposed in water and/or polar solvent (21, 22). In addition, Neon or other gases are not used as pressure-transmitting medium since the phase transition of samples occurs at a very low pressure range, being the order of less than 0.5 GPa, which is easily missed if the gases are

guaranteed to seal in DAC (23). Two ruby balls with diameters being the order of 10 μm were loaded in the sample chamber. The pressure was determined by the ruby luminescence method. Such a pressure method was also employed in other high pressure experiments in this work, including high pressure single crystal X-ray diffraction, high pressure Raman and mid-IR measurements, high pressure optical absorbance measurement, and high pressure static photoluminescence and time-resolved photoluminescence dynamics experiment. GSAS program was employed to refine the obtained experimental XRD profiles (19).

2.3. *In situ* synchrotron single crystal X-ray diffraction at ambient condition and pressures

Single crystal X-ray diffractions at ambient pressure and high pressures were carried out at the experimental station 13-BM-C of the Advanced Photon Source (APS), Argonne National Laboratory (ANL). High quality single crystal samples were loaded in a symmetric-type diamond anvil cell (DAC) with a 56^{o} open angle and a pair of 400 μm culets. A metal gasket was pre-indented to 50 μm in thickness, and then a hole with a diameter of 120 μm was laser-drilled to serve as the sample chamber using a laser micro-matching system (20). The X-ray beam was monochromated with a silicon 311 crystal to 28.6 keV (0.434 Å), with 1 eV bandwidth. A Kirkpatrick-Baez mirror system was used to obtain a vertical × horizontal focus spot size of 15 μm × 15 μm, measured as full width at half maximum (FWHM). The MAR165 Charge Coupled Device (CCD) detector (Rayonix) was placed about 175 mm away from the sample, and ambient LaB_6 powder was used to calibrate the distance and tilting of the detector. The sample was placed on the rotation center of the diffractometer, and was aligned by an optical microscope. For ambient pressure diffraction, a wide rotation exposure covered an angular range from φ=-90 ° to φ=90°, followed by a series of step φ-exposures, each covering 1 ° scan width. For high pressure diffraction, the angular range of the wide rotation exposure was φ=-28° to φ=28°,

limited by the maximum opening angle of the diamond anvil cell (56°), and the scan width of the step φ-exposure was 1°. The typical exposure time was 1s/° for ambient diffraction, and 5s/° for high pressure diffraction. At zero diffractometer position, the φ scan rotation axis for the 13-BM-C diffractometer is in the horizontal plane of the instrument, and is perpendicular to the incident X-ray direction. After the first set of wide and step φ exposures, collected at the zero detector position, similar data were collected with the detector rotated about the horizontal axis (2θ) by 20°, and then with the detector rotated about the vertical axis (ν) by ±10°. The wide rotation exposures were used to extract *d*-spacings, azimuthal angles around the beam center, and peak intensities of each diffraction peak, and the step φ exposures provided the third spatial coordinate necessary for reconstructing the crystal's reciprocal lattice and were used to index the diffraction pattern. The diffraction images were analyzed using the ATREX/RSV software package (24). Polarization, Lorentz, and empirically determined diamond absorption corrections were applied to the fit peaks. The unit cell and orientation matrix were determined in RSV for each data-set. Lattice parameters were refined in RSV using a least-squares fitting procedure. Corrected peak intensities were used to refine the crystal structures with SHELXL software, facilitated by WINGX and Olex2 general user interface (25-27).

2.4. *In situ* high pressure Raman measurements

In situ high pressure Raman measurements were conducted at the Center for High Pressure Science and Technology Advanced Research (HPSTAR), Shanghai. The micro Raman system is based on an optical microscope (Renishaw microscope, equipped with 5x, 20x, 50x and 100x short and long working distance microscope objectives) used to focus the excitation light, an inVia Renishaw microscope and a standard CCD array detector. The sample was loaded in Mao-type symmetric DAC with a pair of 400 μm culets and placed in a rhenium (Re) gasket hole with a diameter the order of 150 μm. Silicon oil was used as pressure transmitting medium which

provided good chemical inertness and hydrostatic condition. A solid laser with a wavelength of 532 nm was used to irradiate the samples. The size of the laser beam was 1-2 μm. Reyleigh scattering light was cut by a Rayleigh filter. The wave-numbers of the Raman shifts were calibrated using single crystalline silicon. The exposure time for a spectrum is 30 seconds. The spectra have been registered in the 80-600 cm^{-1} range.

2.5. *In situ* high pressure synchrotron infrared spectra measurements

In situ high pressure synchrotron infrared spectra measurements were performed at BL01B beamline, Shanghai Synchrotron Radiation Facility (SSRF) (28). The synchrotron IR beam size is focused to a vertical × horizontal focus spot with a size of 20 μm × 20 μm. A short symmetric type diamond anvil cell (DAC) with a thickness of ~25mm and a pair of IIa-type diamond anvils with the culets size of 300 μm were employed. The spectra were recorded by a Nicolet spectrometer with a liquid nitrogen cooled MCT detector. A Re gasket with an initial thickness of 250 μm was preindented in the DAC to a final thickness of ~60 μm, and a 150 μm hole was drilled at the center of the indentation that served as a sample chamber. A small amount of finely KBr was then loaded in the sample chamber and made transparent by gently tightening the DAC. Then a small amount of sample was transferred on to the transparent KBr for high-pressure measurements along with a small ruby ball. The 50 μm sample was used for the synchrotron measurements. Spectral data collection employed a resolution of 1 cm^{-1} and 512 scans. For each pressure, the measurements of background and sample were carried out in the absorption mode.

2.6. *In situ* high pressure optical absorption spectroscopy

In situ high pressure optical absorption spectroscopy was conducted at the experimental station U2A beamline of the National Synchrotron Light Source (NSLS) at Brookhaven National Laboratory (BNL). The visible absorption measurements between 10000 and 25000 cm^{-1} utilized

a customized visible microscope system (29), while the near-IR measurements between 8000 and 11000 cm^{-1} used a Bruker Vertex 80v FT-IR spectrometer coupled to a Hyperion-2000 microscope with a MCT detector and CaF_2 beam splitter. A symmetric type diamond anvil cell (DAC) and a pair of IIa-type diamond anvils with the culets size of 300 μm were employed. KBr was used as pressure transmitting medium and the KBr spectra were used to determine an absorbance baseline.

2.7. *In situ* high pressure photoluminescence measurement

In situ high pressure photoluminescence measurement was conducted at the Center for Nanoscale Materials (CNM), Argonne National Laboratory (ANL). To measure static photoluminescence and time-resolved photoluminescence dynamics, single-crystal and polycrystalline samples were photoexcited at 450 nm and 40 nJ/cm^2 via a 35-ps pulse-width laser diode. PL photons were collected with a lens and directed to a 300-mm focal-length grating spectrograph outfitted with a thermoelectrically cooled CCD and avalanche photodiode with time-correlated single-photon-counting electronics. The sample was loaded in a Mao-type symmetric DAC with a pair of 400 μm culets and placed in a rhenium (Re) gasket hole with diameter being on the order of 200 μm. Silicon oil was used as pressure transmitting medium which provided good chemical inertness and hydrostatic condition.

2.8. First-principles computer simulations

The calculations were performed in the framework of density functional theory (DFT) through the Vienna ab initio simulation package (30). The Generalized gradient approximation (GGA) under Perdew-Burke-Ernzerhof parameterization revised for solids (PBEsol) (31, 32) was implemented to describe the exchange correlation functionalism. The projected-augmented wave potentials were used with 14 valence electrons for Pb ($5d^{10}6s^26p^2$), 7 for I ($5s^25p^2$), 4 for C atoms

($2s^2 2p^2$), 5 for N atoms ($2s^2 2p^3$) and 1 for H ($1s^1$). We used a plane-wave basis set with kinetic 500 eV energy cut off, which is sufficient to optimize the structure until forces acting on each atom are less than 0.02 eV $Å^{-1}$. We employed Monkhorst mesh of 2×2×3 k points for *I4/mcm* phase (low pressure phase of $MAPbI_3$) and 2×2×2 k points for *Imm2* phase (high pressure phase of $MAPbI_3$) with the tetrahedron integration scheme. Their initial crystal structures were introduced from our single-crystal experiments and the atomic position of unresolved light elements are referenced from prior works (33). Our calculation did not incorporate spin-orbit coupling effects, which were considered to alter the electronic band structure (34). However, based on our simulation and as also stated in other GGA-DFT based works (35), the spin-orbit effects was estimated as a small correction to the energy. Pressure was applied by adding Pulay stress to the diagonal elements of the stress tensor. The crystal band structures were sampled along the high-symmetry points in the Brillouin zone.

References

1. Baikie T, et al. (2013) Synthesis and crystal chemistry of the hybrid perovskite $(CH_3NH_3)PbI_3$ for solid-state sensitised solar cell applications. *J Mater Chem A* 1(18):5628-5641.

2. Baikie T, et al. (2015) A combined single crystal neutron/X-ray diffraction and solid-state nuclear magnetic resonance study of the hybrid perovskites $CH_3NH_3PbX_3$ (X = I, Br and Cl). *J Mater Chem A* 3(17):9298-9307.

3. Sheldrick GM (2008) A short history of *SHELX*. *Acta Cryst* A64:112-122.

4. Cardona M (2013) *Raman scattering in materials science*. Vol. 42 (Editors: Weber, Willes H., Merlin, Roberto), Springer Science & Business Media.

5. Quarti C, et al. (2014) The Raman Spectrum of the $CH_3NH_3PbI_3$ Hybrid Perovskite: Interplay of Theory and Experiment. *J Phys Chem Lett* 5(2):279−284.

6. Niemann RJ, et al. (2016) Halogen effects on ordering and bonding of $CH_3NH_3^+$ in $CH_3NH_3PbX_3$ (X = Cl, Br, I) hybrid perovskites: a vibrational spectroscopic study. *J Phys Chem C* 120(5):2509-2519.

7. Oxton IA, Knop O, Duncan JI (1977) The infrared spectrum and force field of the methyl-ammonium ion in $(CH_3NH_3)_2PtCl_6$. *J Mol Struct* 38:25-32.

8. Flender O, Klein JR, Lenzer T, Oum K (2015) Ultrafast photoinduced dynamics of the organolead trihalide perovskite $CH_3NH_3PbI_3$ on mesoporous TiO_2 scaffolds in the 320-920 nm range. *Phys Chem Chem Phys* 17(29):19238-19246.

9. Onoda-Yamamuro N, Matsuo T, Suga H (1990) Calorimetric and IR spectroscopic studies of phase transitions in methylammonium trihalogenoplumbates (II). *J Phys Chem Solids* 51(12):1383-1395.

10. Glaser T, et al. (2015) Infrared Spectroscopic Study of Vibrational Modes in Methylammonium Lead Halide Perovskites. *J Phys Chem Lett* 6(15):2913-2918.

11. Jaffe A, Lin Y, Mao WL, Karunadasa HI (2015) Pressure-Induced Conductivity and Yellow-to-Black Piezochromism in a Layered Cu–Cl Hybrid Perovskite. *J Am Chem Soc* 137(4):1673–1678.

12. Tauc J (1968) Optical properties and electronic structure of amorphous Ge and Si. *Mater Res Bull* 3(1):37-46.

13. Fox M (2010) *Optical Properties of Solids*, Oxford University Press, Oxford.

14. Strobel TA, et al. (2011) High-pressure study of silane to 150 GPa. *Phys Rev B* 83(14):144102.

15. Shi D, et al. (2015) Low trap-state density and long carrier diffusion in organolead trihalide perovskite single crystals. *Science* 347(6221):519-522.

16. Lee MM, Teuscher J, Miyasaka T, Murakami TN, Snaith HJ (2012) Efficient Hybrid Solar Cells Based on Meso-Superstructured Organometal Halide Perovskites. *Science* 338(6107):643-647.

17. Jiang Q, Sheng X, Li Y, Feng X, Xu T (2014) Rutile TiO_2 nanowire-based perovskite solar cells. *Chem Commun* 50(94):14720-14723.

18. Lee PL, et al. (2008) A twelve-analyzer detector system for high-resolution powder diffraction. *J Synchrotron Rad* 15(5):427-432.

19. Larson AC, von Dreele RB (1994) *General structure analysis system (GSAS).* Los Alamos National Laboratory Report LAUR 86-748.

20. Hrubiak R, Sinogeikin S, Rod E, Shen G (2015) The laser micro-machining system for diamond anvil cell experiments and general precision machining applications at the High Pressure Collaborative Access Team. *Rev Sci Instrum* 86(7):072202.

21. Im JH, Jang IH, Pellet N, Grätzel M, Park NG (2014) Growth of $CH_3NH_3PbI_3$ cuboids with controlled size for high-efficiency perovskite solar cells. *Nature Nanotech* 9(11):927–932.

22. Zhou Y, et al. (2015) Room-temperature crystallization of hybrid-perovskite thin films *via* solvent–solvent extraction for high-performance solar cells. *J Mater Chem A* 3(15):8178-8184.

23. Rivers M, et al. (2008) The COMPRES/GSECARS gas-loading system for diamond anvil cells at the Advanced Photon Source. *High Pressure Res* 28(3):273–292.

24. Dera P, et al. (2013) High pressure single-crystal micro X-ray diffraction analysis with GSE_ADA/RSV software. *High Pressure Res* 33(3):466-484.

25. Dolomanov OV, Bourhis LJ, Gildea RJ, Howard JAK, Puschmann H (2009) *OLEX2*: a complete structure solution, refinement and analysis program. *J Appl Cryst* 42(2):339-341.

26. Farrugia LJ (2012) *WinGX* and *ORTEP for Windows*: an update. *J Appl Cryst* 45(4):849-854.

27. Sheldrick GM (2008) A short history of *SHELX*. *Acta Cryst* A64(1):112-122.

28. Zhang Z, et al. (2014) Performance of the infrared microspectroscopy station at SSRF. *Infrared Phys Techn* 67:521-525.

29. Jaffe A, Lin Y, Mao WL, Karunadasa HI (2015) Pressure-induced conductivity and yellow-to-black piezochromism in a layered Cu–Cl hybrid perovskite. *J Am Chem Soc* 137(4):1673–1678.

30. Kresse G, Hafner J (1994) *Ab initio* molecular-dynamics simulation of the liquid-metal amorphous-semiconductor transition in germanium. *Phys Rev B* 49(20):14251-14269.

31. Perdew JP, Burke K, Ernzerhof M (1996) Generalized gradient approximation made simple. *Phys Rev Lett* 77(18):3865-3868.

32. Perdew JP, et al. (2008) Restoring the density-gradient expansion for exchange in solids and surfaces. *Phys Rev Lett* 100(13):136406.

33. Oku T (2015) *Solar Cells - New Approaches and Reviews*, pp. 78-101, InTech, Rijeka.

34. Even J, Pedesseau L, Jancu JM, Katan C (2013) Importance of spin–orbit coupling in hybrid organic/inorganic perovskites for photovoltaic applications. *J Phys Chem Lett* 4(17):2999-3005.

35. Colella S, et al. (2013) $MAPbI_{3-x}Cl_x$ Mixed halide perovskite for hybrid solar cells: the role of chloride as dopant on the transport and structural properties. *Chem Mater* 25(22):4613-4618.